OPEN ACCESS
IOP Publishing
Superconductor Science and Technology
Supercond. Sci. Technol. **36** (2023) 053001 (23pp)
https://doi.org/10.1088/1361-6668/acbb35

Topical Review

Modelling high-T_c electronics

Colin Pegrum

Department of Physics, University of Strathclyde, Glasgow G4 0NG, United Kingdom

E-mail: colin.pegrum@strath.ac.uk

Received 19 August 2022, revised 19 January 2023
Accepted for publication 10 February 2023
Published 9 March 2023

Abstract

This Review examines methods to model Josephson devices such as arrays of superconducting quantum interference devices (SQUIDs) and rows within two-dimensional superconducting quantum interference filters or SQIFs. The emphasis is on high temperature superconducting (HTS) devices, though the techniques apply for any operating temperature. The methods use freely-available and proven software to first extract all self and mutual inductances of the thin-film device, and then to incorporate these data, plus junction models and thermal noise sources into an equivalent circuit for Josephson simulation. The inductance extraction stage also estimates the effective areas of each loop in a structure and also the variation of inductance as temperature changes, due to the varying penetration depth. The final post-processing stage can yield current–voltage, voltage-field and field spectral density responses. The Review also touches briefly on the simulation of a simple model for a terahertz single-junction HTS mixer and also looks at the behaviour of typical hysteretic and non-hysteric HTS RF SQUIDs.

Keywords: superconductor, HTS, Josephson, simulation, inductance extraction, SQUID, SQIF

(Some figures may appear in colour only in the online journal)

1. Introduction

This Review sets out some methods for modelling high transition temperature (HTS or high-T_c) superconducting devices with wide-ranging applications, such as SQUID arrays and parts of SQIFs. A single SQUID or superconducting quantum interference device has one loop and two junctions. A SQUID array has N identical loops in parallel and $N+1$ junctions. A SQIF or superconducting quantum interference filter is similar to a SQUID array, but differs in one key aspect: its loops have a controlled and random spread of areas. This results in a voltage-field or $V(B)$ response which has one, sharp minimum, unlike SQUIDs which have multiple periodic minima. For overviews and details of SQUIDs and SQIFs see [1–4].

The emphasis in this Review is on single-layer HTS devices but all the methods are applicable to LTS or low-T_c as well. Section 2 briefly reviews the basic properties of Josephson junctions, including a junction model, connections of junctions in a closed loop, thermal noise and the underlying equations describing junction dynamics. The overall flow of modelling and simulation is set out in section 3; it has two main stages—deriving the inductances of all parts of a thin-film device (inductance extraction) and Josephson simulation. Section 4 focuses on inductance extraction, the effective areas A_{eff} of structures and the temperature dependence of inductance. Section 5 outlines the various software packages available for Josephson simulation. Post-processing of the data is covered in section 6 to produce current–voltage or $I-V$ curves, the response to magnetic field $V(B)$ and also power spectral density (PSD) data. In some cases the extraction package `FastHenry` can be used and examples of these are set out in section 7, with simulation results and comparison with fabricated SQUID arrays. Other devices need extraction by `3D-MLSI`; this is covered in section 8. Section 9 discusses the

unique form of the $I-V$ curve for long arrays and SQIF rows. Single-junction microwave mixers are outlined in sections 10 and 11 deals with RF SQUIDs. The final section touches briefly on an alternative Josephson simulation method based on electronic analogues. The Appendices cover other inductance extraction programs, a collection of analytical expressions for self inductance, Verilog-A junction models and an example using the partial element equivalent circuit concept.

2. Josephson junctions

These are usually made from two thin films of superconductor coupled weakly through a small localised barrier, weak link or bridge. For multi-layer LTS junctions this is frequently a native insulating oxide, but HTS junctions are normally patterned from a single film and the barrier is an intrinsic region of weakly-superconducting material, such as in a step-edge, bi-crystal or ramp junction. See for example [5, 6] for practical details of such junctions.

If the coupling through the junction is sufficiently weak the superconducting wave-functions either side of it overlap and quantum tunnelling of electron pairs allows a supercurrent I to flow without voltage across the junction, up to some critical current I_{cj}. It can be shown [7, 8] that

$$I = I_{cj}\sin\phi \tag{1}$$

where ϕ is the difference of the superconducting phases across the junction. Equation (1) describes the DC Josephson effect and for $I < I_{cj}$ the junction is in the zero-voltage or static state. For $I > I_{cj}$ a time-varying voltage $V(t)$ appears across the junction, related to the phase difference ϕ:

$$\frac{\mathrm{d}\phi}{\mathrm{d}t} = \frac{2\pi}{\Phi_0}V(t). \tag{2}$$

This is the AC Josephson effect. The flux quantum is $\Phi_0 = h/2e$, where h is Planck's constant and e the electron charge. Integration with respect to time gives a voltage average:

$$\phi(t) = \frac{2\pi}{\Phi_0}\int_0^t V(t')\mathrm{d}t' = \frac{2\pi\,\overline{V(t)}}{\Phi_0}t \tag{3}$$

so the phase evolves steadily with time. Substituting equation (3) in equation (1) the current oscillates as

$$I = I_{cj}\sin(2\pi ft) \tag{4}$$

where the frequency$f = \overline{V(t)}/\Phi_0 \equiv 0.484\,\mathrm{GHz}\,\mu\mathrm{V}^{-1}$. So the Josephson junction in its dynamic state with $I > I_{cj}$ may have $V(t)$ oscillating in the GHz or THz range, but what is measured in the laboratory for analogue Josephson devices is almost always the time-average $\overline{V(t)}$.

2.1. The RCSJ model for a single junction

There are two additional conduction paths in parallel with the Josephson current equation (1): a resistive current through a parallel shunt R_j and a displacement current through the junction capacitance C_j. The total junction current I is then

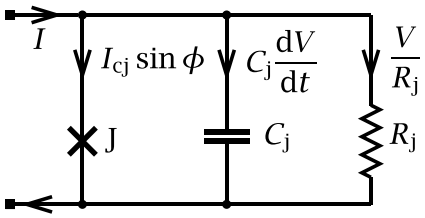

Figure 1. The RSCJ model of a single junction, as defined by (5). J denotes the junction.

$$I = I_{cj}\sin\phi + \frac{V}{R_j} + C_j\frac{\mathrm{d}V}{\mathrm{d}t} \tag{5}$$

$$= I_{cj}\sin\phi + \frac{\Phi_0}{2\pi R_j}\frac{\mathrm{d}\phi}{\mathrm{d}t} + \frac{C_j\Phi_0}{2\pi R_j}\frac{\mathrm{d}^2\phi}{\mathrm{d}t^2}. \tag{6}$$

This is the RCSJ or Resistively- and Capacitively-Shunted Junction model. Φ_0 is the flux quantum. For analogue devices that operate at voltages much less than the superconducting gap voltage, R_j can usually be safely assumed to be linear. More generally, the sub-gap resistive channel is non-linear, and a more complex model may be needed [9, 10]. The RCSJ can be represented by the equivalent circuit in figure 1.

A junction may have a hysteretic current–voltage ($I-V$) curve: for $I < I_{cj}$, the junction can be in one of two states, with $V = 0$ or $V \neq 0$ (see section 2.1.1 in [1]). For analogue applications such hysteresis is generally undesirable and is suppressed by choosing the shunt resistance R_j so that the Stewart–McCumber parameter $\beta_C = (2\pi I_{cj}{R_j}^2 C_j)/\Phi_0 < 1$ [11, 12].

For LTS junctions R_j would be added by patterning a separate normal-metal layer at the fabrication stage. But for most HTS junctions the material forming the junction creates a built-in shunt, for example the upper edge of a step-edge junction [13]. For these the shunt and normal resistances are assumed equal and we will use R_{nj} (measured for $I >> I_{cj}$) as the parallel resistance in (1). Most HTS junctions are intrinsically non-hysteretic and generally have $\beta_c \ll 1$.

2.2. Junctions in a loop

In a closed loop of superconductor there is an extra constraint: the single-valued nature of the wave-function requires the phase change around the loop to be modulo 2π. For a loop which has for example two junctions this leads to [14, 15]

$$\phi_1 - \phi_2 = 2\pi\Phi_L/\Phi_0 \tag{7}$$

where ϕ_1 and ϕ_2 are the junction phase differences and Φ_L is the total magnetic flux within the loop. A 2-junction loop like this is the classic DC SQUID [16]. A key parameter for a loop of inductance L is the modulation parameter $\beta = 2LI_{cj}/\Phi_0$. It is relevant for not only single-loop two-junction devices like the DC SQUID, but also for loops within SQUID arrays and SQIFs.

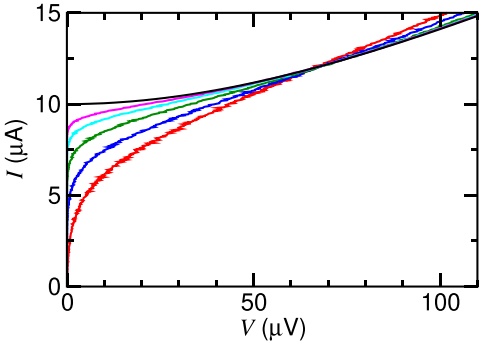

Figure 2. Simulated noise-rounded $I-V$ curves for $\Gamma = 0.32, 0.16, 0.08, 0.04, 0.02$ and 0 (lower to upper). $I_{cj} = 10\,\mu$A, $R_{nj} = 10\,\Omega$, $C_j = 18$ fF. $\Gamma = 0.32$ corresponds to $T \approx 77$ K.

2.3. Thermal noise

HTS Josephson devices operate from around 40 to 77 K and two significant effects due to thermal fluctuations must be considered. The shunt resistors generate Nyquist noise that can be modelled by current-noise sources in parallel with each R_{nj}, with spectral density $S_I = 4k_BT/R_{nj}$, where T is absolute temperature and k_B is Boltzmann's constant. For a single junction this causes noise-rounding of the junction's $I-V$ curve [17]. The degree of rounding is set by the parameter $\Gamma = (2\pi k_BT)/(I_{cj}\Phi_0)$, which compares thermal energy to Josephson coupling energy. Figure 2 shows simulations for a range of Γ values. The rounded $I-V$ curves for a single junction with zero capacitance can also be calculated [17, 18].

In addition, for a DC SQUID with inductance L, its magnetic energy for one flux quantum, $\Phi_0^2/2L$, must be much greater than k_BT. One convention [5, 19] is to define a thermal inductance L_{th} as $(\Phi_0^2)/(4\pi k_BT) = 320$ pH at $T = 77$ K; alternatively, in [20–22] L_{th} is defined as $(\Phi_0^2)/(4\pi^2 k_BT) = 102$ pH at $T = 77$ K. Either way, this adds the constraint $L \ll L_{th}$ and so it is clear that inductances in HTS SQUIDs and other devices at 77 K should be much less than ≈ 100 pH.

The parameters Γ and L_{th} are important for the noise-rounding of the $I-V$ curves of SQUID arrays and SQIF rows, as covered later in sections 8.1 and 8.2.

2.4. Special features of a Josephson junction

Circuits containing Josephson junctions have unique features that set them apart from those with just passive elements and semiconductor devices. Each junction is described by a second-order non-linear differential equation equation (5). This means that in almost all cases numerical methods or custom software packages are needed to find solutions for $V(t)$. The exception is a single junction with $C_j = 0$, when equations (2) and (5) can be integrated and then $\overline{V(t)}$ has a parabolic dependence on current:

$$\overline{V(t)} = I_{cj}R_{nj}\sqrt{(I/I_c)^2 - 1} \qquad (8)$$

which for $T = 0$ is the $\Gamma = 0$ $I-V$ curve in figure 2.

There is also the concept of superconducting phase and its connection with flux in closed loops, as given in equation (7). And it is essential to be aware of the timescale: a current $I > I_{cj}$ will create oscillations with nano- or pico-second periods, as set by equation (4).

2.5. Solving equations for multi-junction devices

The devices to be considered later generally have n junctions in parallel, to form an array of $(n+1)$ equal-area loops, or a SQIF with a random spread of loop areas. We use I_{cj} and I_{ca} as junction and array critical currents, so $I_{ca} = nI_{cj}$ and similarly $R_{na} = R_{nj}/n$. The fabrication process aims to make junctions all with the same I_{cj} and R_{nj} values, though it is straightforward to introduce some statistical spread in these parameters to represent real fabricated devices.

The *ab initio* approach is to use equations (2) and (5) for each junction, plus the constraint on flux and phase differences in equation (7) for closed loops, plus the usual Kirchhoff's rules for voltages around loops and currents at nodes, add in uncorrelated current-noise sources for each R_{nj} and solve the resulting set of ordinary differential equations (ODE's) by an appropriate method. This can be by custom code, or MatLab or Octave are alternatives.

There is a large body of work in the literature on solving these equations for DC SQUIDs including the effects of noise, starting with the seminal work by Tesche and Clarke for the first Nb LTS SQUIDs [15, 23]. The methods have been extended to HTS SQUIDs, allowing for the greater levels of thermal noise, see for example [5, 19, 21, 22, 24].

For devices like SQUID arrays and SQIFs it is still possible in principle to solve a set of ODE's [25]. But for multi-loop, multi-junction devices, possibly with a designed spread of loop inductances and a random spread of I_{cj} and R_{nj}, this becomes increasingly more difficult. It is also important to include mutual inductance. For SQIFs it is necessary to determine the effective area, to get the true response to an external magnetic field, and the self-field created by bias currents flowing through the structure can also be significant. This is where it becomes useful or indeed essential to turn to packages that can extract all inductances for the actual physical layout and feed these into custom Josephson modelling software. This Review follows this route.

3. The overall modelling flow

Figure 3 outlines the procedures described in the sections to follow. From design data for the device (geometry, film thickness, value of the penetration depth λ at the chosen operating temperature) a text file is created and input to an inductance extractor, section 4, which outputs an inductance matrix $\mathbf{L}$. At the inductance extraction stage the effective areas of individual loops in a SQUID array or SQIF can be estimated.

The values of self and mutual inductances from $\mathbf{L}$ are merged computationally with text specifying the Josephson junctions, current sources and other information for Josephson simulation (section 5). The latter will usually step through

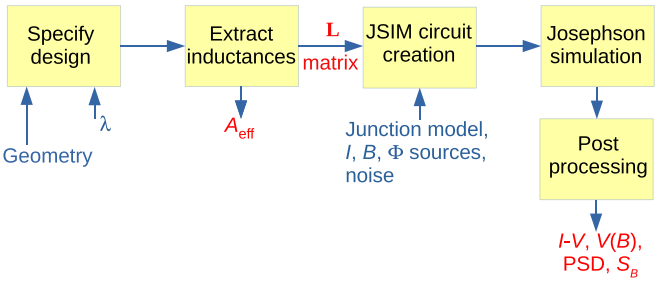

Figure 3. The complete inductance extraction and simulation process using `JSIM`.

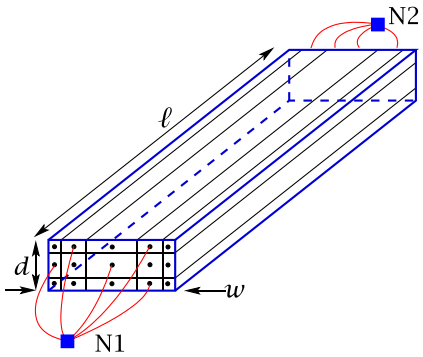

Figure 4. `FastHenry` segment discretisation. In this example `nwinc` = 5 and `nhinc` = 3. Connections shown as dots at the ends of the 15 filaments are connected to nodes N1 and N2, marked as ■. For clarity only a few connections are shown and the nodes are actually located at the centres of the end faces of the segment.

a nested range of control parameters, such as I_b, T and a field-generating current to create an applied magnetic field B. Parallel processing greatly reduces the computational time for this stage. The simulation output will be a noisy time-varying voltage $V(t)$ and this data is post-processed (section 6) to give $I-V$ curves and the $V(B)$ response. There is also the option to take the PSD to find the field spectral density S_B for arrays and SQIFs, or the frequency spectrum for single-junction mixers. Extracting a PSD generally requires a longer run of time-domain data than is needed for $I-V$ curves or $V(B)$.

4. Inductance extraction

We will discuss in detail two freely-available packages for inductance extraction: `FastHenry` and `3D-MLSI`. Some other specialised techniques will also be mentioned briefly. This Review will focus primarily on relatively simple HTS devices such as single-junction mixers, SQUIDs, SQUID arrays and parts of SQIFs. These are single-layer structures with no groundplane, which simplifies inductance extraction (though `3D-MLSI` can include groundplanes if required, as can `FastHenry` to a limited extent).

4.1. *FastHenry*

`FastHenry` was developed originally to find the frequency-dependent impedances of normal-metal tracks and wires in interconnections in chip and board-level semiconductor circuitry [26, 27]. It decomposes a thin-film structure into an interconnected network of N_s straight segments with rectangular cross sections. Each segment, *i.e.* a thin-film track of thickness d, width w and length ℓ is then discretized into thin filaments, as in figure 4. There are `nhinc` filaments across the width and `nwinc` through the thickness. The discretisation is finer at surfaces, as this is where high-frequency currents would flow for normal metals, controlled by the skin depth. By default a filament differs in thickness or width from its outer neighbour by a factor of two which can be changed using the `rh` and `rw` parameters. There is a concise introduction to `FastHenry` with examples in its User's Guide [28].

The `FastHenry` code was extended by Whiteley [29] to allow for superconducting films using a two-fluid model for supercurrent flow. Note that this model *does* include kinetic inductance (see comments in [30]). Specifying a non-zero λ for a segment causes it to be analysed as a superconductor, or λ can be set as a global default and then all conductors are superconducting. The degree of discretisation needed depends on the values of d and w compared to λ, see section 4.1.1.

The ends of all filaments in a segment are joined electrically to its two nodes (or ports) and current flows between these nodes—N1 and N2 in figure 4. `FastHenry` determines the partial self impedance of each segment in the network and their mutual impedance to each of the other segments. So it generates an $N_s \times N_s$ impedance matrix for a collection of N_s 2-port segments or tracks. For an all-superconducting structure the real parts of the impedances are zero and if the frequency is set to $(1/2\pi)$ Hz the magnitudes of the imaginary parts are the inductances.

`FastHenry` and the manner in which it is used is based on the concept of partial element equivalent circuits or PEEC [27, 31]. We will return to this in more detail in section 7.

The inherent rectilinear nature of `FastHenry` imposes constraints and limitations on the types of thin-film geometries that yield accurate and dependable extracted inductances using it. It is important to be aware of these. Essentially, there are two issues: segment or track lengths ideally need to be much longer than the track width, and corners can be a problem. Some trivial comparisons will illustrate these points.

Firstly, the loop in figure 5 has all track widths substantially less than the loop dimensions. It is a continuous structure defined by nodes 1–5. `FastHenry` gives $L_{15} = 36.6\,\text{pH}$ between the external ports 1 and 5, for a $0.22\,\mu\text{m}$ film with $\lambda = 0.3\,\text{nm}$. This is within 1% of values found by other inductance extraction methods.

On the other hand, the loop structure in figure 6(a) is much more difficult to specify realistically in `FastHenry`. Other techniques we will look at later estimate its true inductance as $L = 18\,\text{pH}$. Figures 6(b)–(d) illustrate the problem: all these have the same inner dimensions, but because its tracks are broad and short, there are several simplistic ways to try to connect their corners. The values of L are either over- or under-estimates, because the current paths at corners are not physically realistic. Remember also that the ends of the filament bundles in each segment are all joined to a common node at

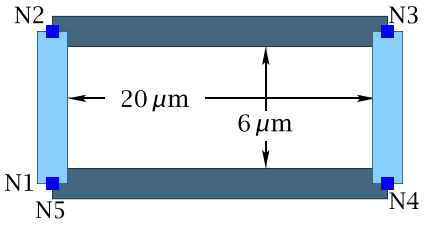

Figure 5. Simple `FastHenry` representation of a loop with 2 μm wide tracks. The loops in the small arrays that will be considered later in section 7.1 have the same dimensions. Nodes N1 and N5 are the external connections.

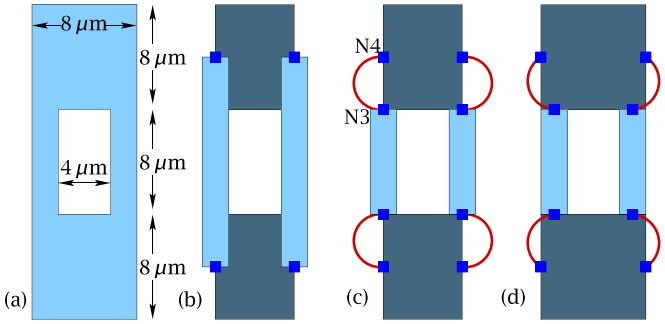

Figure 6. (a) Loop geometry. (b) A simple `FastHenry` representation. The four strips share four nodes (■). In (c) and (d) each track has its own pair of nodes, and nodes like N3 and N4 are made 'equivalent', shown as red links, so for example current flows out of N3 and into N4 via an inductance-less path. Inductances from `FastHenry`, using $\lambda = 300$ nm and a film thickness of 220 nm are (b) 25.3 pH (c) 13.5 pH and (d) 15.1 pH.

one point in space, so current diverges unrealistically from each node into the body of the segment. This difficulty can be overcome partially by sub-dividing broad tracks at corners and elsewhere into an interconnected mesh of small `FastHenry` segments, as first proposed in [32].

Fourie *et al* have taken this concept very much further with their `InductEx` program [30, 33, 34]. This started life as front-end to `FastHenry`, taking data from GDS II files specifying the layout and then sub-dividing it into a mesh of rectangular sub-segments, with sizes, interconnections and discretisation to match the expected current flow in the structure.

Complex structures like this can run exceedingly slowly through `FastHenry` and the Stellenbosch project has evolved, firstly to make changes to the `FastHenry` code to allow for multi-port networks and to increase its speed for structures with many inductors (so-called `Fast FastHenry` or `FFH`) [35, 36]. Subsequently the segmentation shape was changed from rectangular to tetrahedral, [36, 37] which deals much better with real 3D structures that the original `FastHenry` could handle. This work is targeted mainly at low-T_c Nb multilayer digital devices for commercial applications [38–41] which is outside the remit of this Review. `InductEx` is available commercially [42]. In this Review we restrict our use of `FastHenry` without any add-ons, for situations where its limitations are not an issue.

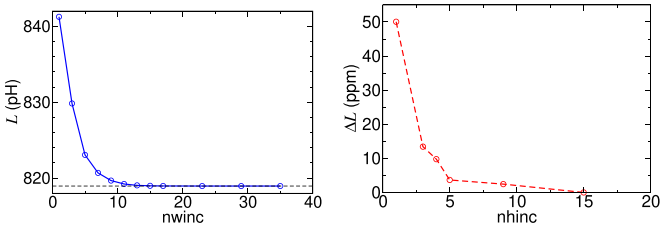

(a) `nhinc` = 3 (b) `nwinc` = 15

Figure 7. Changing the number of filaments for a track 1000 μm long, 50 μm wide and 200 nm thick, with $\lambda = 90$ nm. A wide track width and a small λ have been chosen for this example.

4.1.1. Discretisation errors. `FastHenry` adjusts the filament density to be highest at surfaces and edges where the current density is greatest. It leaves the user to choose the actual number of filaments, set by statements like `nhinc = 5` and `nwinc = 7`. Too few filaments results in inductance errors; an excessive number needlessly slows down the calculation and may even exceed the memory available. So what values to choose?

If λ is comparable with the film thickness d, then the current density does not vary greatly through the film thickness and setting `nhinc` to no more than 3 or 5 will give adequate accuracy. But the width w of a segment may be much greater than λ and many more filaments are needed across the width. It is always useful to first run simple tests for a range of values of `nhinc` and `nwinc` for a representative segment. Figure 7 shows this for a single segment, where it is clear the inductance only attains its limiting value for this example for `nwinc` ≈15. Yet as expected there is very little dependence on the value of `nhinc`.

4.1.2. Inductance matrix asymmetry. For a set of N_s separate segments `FastHenry` generates an $N_s \times N_s$ impedance matrix. The imaginary parts of the diagonal elements are the self terms like L_{11}, $L_{22}, \ldots$ and those like L_{12}, $L_{13}, \ldots$ are the mutuals. Sometimes these off-diagonal terms are inconsistent, for example $L_{12} \neq L_{21}$. Ideally they should be equal. The error is usually small and can be further reduced by increasing the multi-pole expansion order from the default value of 2, with only a very slight increase in computing time. A perfectly symmetric matrix should result from switching to a different method of matrix manipulation within `FastHenry` using `-s ludecomp`, though this can run more slowly.

4.2. *3D-MLSI*

This program is due to Mikhail Khapaev and colleagues at Moscow State University [43–46]. It uses a text file to specify the thin-film structure, which can be multi-layered in x–y planes. All films are treated as superconductors, so unlike `FastHenry`, it generates an inductance matrix rather than an impedance matrix. It has several other features, such as visualisation of current flow and the inclusion of external fields. It is freely available as a set of 32-bit Windows binaries with a short user manual [47].

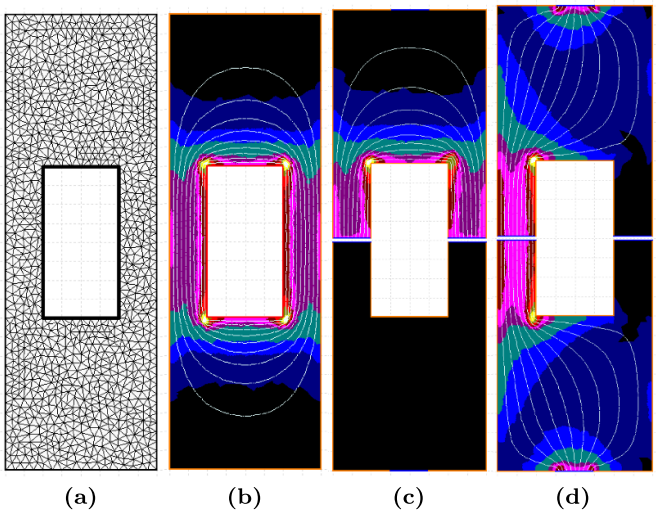

Figure 8. `3D-MLSI` for the figure 6(a) structure. (a) The FEM mesh, (b) closed-loop model, (c) and (d) split-loop model. (c) Depicts the current streamline and field solution for the part of the current that flows around the upper half (the lower half looks the same) and (d) is for the flow between the terminals at the upper and lower edges. In (c) and (d) the gaps have been enlarged for clarity (These gaps also have terminals, which would connect to Josephson junctions in the complete simulation model.).

`3D-MLSI` uses a finite element method (FEM) with a triangular mesh and so can cope very effectively with corners and irregular structures. It generates a finer mesh automatically where current density will be higher, at edges and corners. Thin-film areas are specified by the x–y co-ordinates of vertices. Boundaries between vertices can be straight lines or arcs. Currents to create flux and extract inductances can be fed into and out of terminals, which can be all or part of a straight boundary. Current flow through each terminal is uniform and perpendicular to its length. An area can have N holes and, if it has no terminals, the structure is treated as a set of N loops and the self and mutual inductances associated with current flow around and between the holes are calculated as an $N \times N$ inductance matrix.

Figure 8 depicts `3D-MLSI` for the structure in figure 6(a). Figure 8(a) is the FEM mesh treating it as a *closed* structure with one hole. Figure 8(b) shows the current streamlines around this hole and the self-field generated. This configuration has no external terminals. In figures 8(c) and (d) the same loop has been split, with terminals added at the top and bottom. These split-loop and closed-loop `3D-MLSI` models have been used to simulate arrays and SQIFs with broad electrodes [48–50]; this is covered in section 8.1.

Some enhancements have been made more recently to `3D-MLSI` to include internal current sources [51]. This is mainly relevant to multi-layer rapid single flux quantum or RSFQ devices and is not addressed in this Review.

4.3. Other inductance extraction and calculation methods

Some of these are outlined in appendix A.

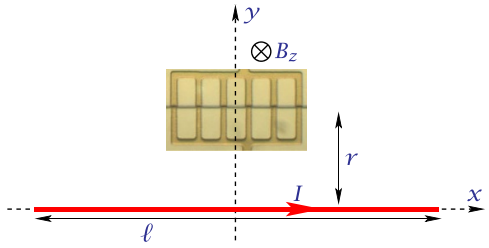

Figure 9. Simulated generation of field B_z though the plane of an array by a current I in a long track.

4.4. Magnetic field response

One of the key objectives of the processes described in the Review is to simulate the response of any device to a uniform magnetic field, usually the voltage-field or $V(B)$ response. It can be generated by an extra track or coil in the layout (not present in the physical device) that creates a field with adequate uniformity.

Figure 9 shows the concept. Here a single long wire creates field $B_z = \alpha I$, with α a constant. The wire length ℓ and spacing r need to be several times the largest dimension of the device. It is straightforward to derive α at the centre of the device and to assess and control its variation over the device using Biot and Savart. A pair of long wires improves uniformity, or better still, a rectangular Helmholtz coil can be used [52]. This creates a volume of near-uniform field that covers the device footprint and also extends above and below its plane, which is needed for devices with significant flux focussing [53].

4.5. Effective areas

Loops with narrow tracks like figure 5, which may be part of SQUID arrays or small SQIFs, each have an effective area $A_{\rm eff}$ very nearly equal to the area defined by lines along the centres of the tracks, since an external field will diverge almost symmetrically around a narrow track. But for structures with broad tracks like figure 6(a), this is not so. Due to flux focussing $A_{\rm eff}$ lies somewhere between the area $A_{\rm h}$ of the central hole and the area $A_{\rm p}$ defined by the outer edges or perimeter. To assess the true field response of devices with loops like this, $A_{\rm eff}$ needs to be known. It can be found easily at the inductance extraction stage (figure 3) from the mutual inductance $M_{\rm f}$ between the loop and the field-generating inductor:

$$A_{\rm eff} = \frac{\Phi}{B_z} = \frac{M_{\rm f} I}{B_z} = \frac{M_{\rm f}}{\alpha} \tag{9}$$

where Φ is the flux induced by I in the loop. Empirically it has been found that

$$A_{\rm eff} = \gamma_{\rm A} \sqrt{A_{\rm h} A_{\rm p}} \tag{10}$$

where $\gamma_{\rm A}$ is a geometry-dependent factor, of the order of unity. For square Nb washer-style SQUIDs Ketchen *et al* [53] found $\gamma = 1$. More recently Drung [54] looked at square, round and polygonal SQUIDs (though *not* rectangular ones) and also found $\gamma \approx 1$.

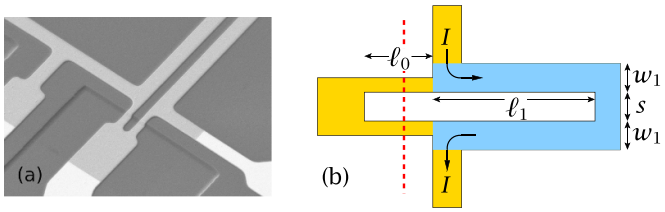

Figure 10. (a) SEM of part of a SQUID with step-edge junctions 2 μm wide. (b) The SQUID model. Injected current I flows through the coupled part shown in blue, which has inductance L_{co}. The red dashed line indicates the step edge.

We will return later to the issue of A_{eff} and values of γ_A for specific examples.

4.6. Temperature dependence of inductance

Accurate simulation and pre-fabrication design need the inductances of all parts of a device to be well-known at the planned operating temperature T. These depend on T due to changes in the penetration depth $\lambda(T)$. There are two inductance contributions: geometric L_{geo} and kinetic L_k. L_{geo} arises from internal and external magnetic energy. It depends on the geometry of the structure and has a weak dependence on $\lambda(T)$. L_k comes from the inertia of superconducting electron pairs and has a strong dependence on $\lambda(T)$. For a single isolated line $L_k \approx (\mu_0\lambda^2)/wt$ per unit length [55], where μ_0 is the magnetic permeability and w and t are its width and thickness. For more complex structures it is challenging to calculate L_k accurately and for these `3D-MLSI` can be used to extract the total inductance $L_{geo} + L_k$ at some temperature T, providing $\lambda(T)$ is known. Note that λ is a user-defined parameter for `3D-MLSI` (and also for `FastHenry`) but its temperature variation is *not* an in-built function for either extractor.

There has been a number of measurements of λ at a fixed temperature [56, 57] by directly measuring the inductance of part of a SQUID loop using current injection. Very recent measurements [58] to find $\lambda(77)$ and $\lambda(T)$ for $50 < T < 79$ K have been made on SQUIDs like figure 10:

These are the type used in directly-coupled magnetometers [59] but here no magnetometer loop is present. A current I is injected through the blue part of the loop and from the flux change measured by the SQUID itself its partial inductance L_c is found. Five different sets of SQUIDs were used at 77 K. Each set had differing values of w_1 and s. One set had $t = 220$ nm and the other four sets were 133 nm thick. Each set had four SQUIDs with different lengths ℓ_1, which enabled the inductance per unit length L_0 to be found for each set. `3D-MLSI` was then used to extract L_0 for the blue structure in figure 10(b) over a range of λ values. By comparing these with the measured $L_0\lambda(77)$ was determined to be 391 nm averaged across all five sets, independent of t.

But it is also desirable to know $\lambda(T)$ over the range attainable by small cryocoolers, as these are being increasingly used to cool devices below 77 K to enhance performance. The lack of published data for $\lambda(T)$ prompted Keenan *et al* [58] to make cryocooler measurements of $L_{co}(T)$ on three different SQUIDs

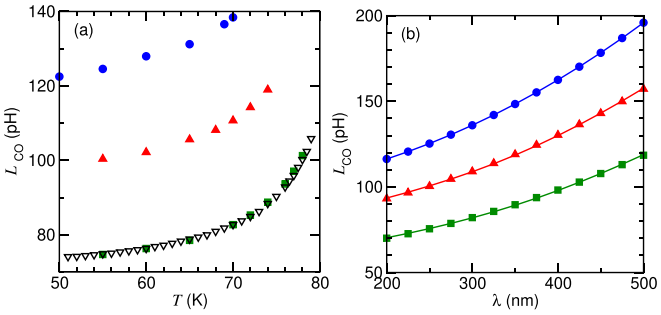

Figure 11. (a) Measured inductance L_{co} as a function of temperature T for SQUIDs with three values of ℓ_1: ● 125 μm; ▲ 100 μm; ▽ and ■ 75 μm. (b) L_{co} extracted by `3D-MLSI`, varying λ for the same SQUIDs; solid lines are cubic fits.

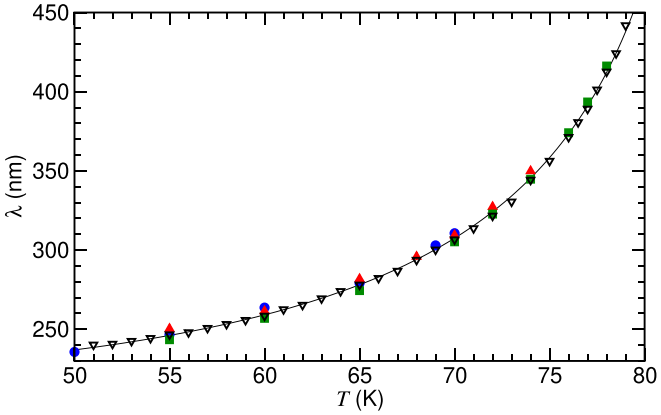

Figure 12. $\lambda(T)$ derived from the data shown in figures 11(a) and (b) for the same three SQUIDs. Data markers are the same as those in figure 11. The solid line is a fit to (11) with $T_c = 86.5$ K.

with $\ell_1 = 125$, 100 and 75 μm and $s = w_1 = 4\,\mu$m, from 50 to 78 K. Figure 11(a) shows the significant change in L_{co}.

L_{co} was then extracted by `3D-MLSI`, stepping λ from 200 to 500 nm, figure 11(b). This data was merged with the experimental values of $L_{co}(T)$ to create a dataset for $\lambda(T)$. This is reasonably expected (*e.g.* [60]) to have the form

$$\lambda(T) = \lambda(0)\left[1 - (T/T_c)^P\right]^{-1/2} \qquad (11)$$

and figure 12 shows a good fit to equation (11), with $\lambda(0) = 217$ nm and $P = 3.36$.

The changing $\lambda(T)$ also changes A_{eff}, figure 13. The changes are modest, but can be significant around 77 K, where temperature fluctuations in liquid nitrogen can potentially add noise when operated in a magnetic field, due to A_{eff} fluctuations [61]. The effect is more pronounced in loops with broad tracks like figure 6(a).

5. Josephson simulation packages

5.1. `WRspice`

The history of `WRspice` can be traced back to the original Berkeley SPICE (simulation program for integrated circuit

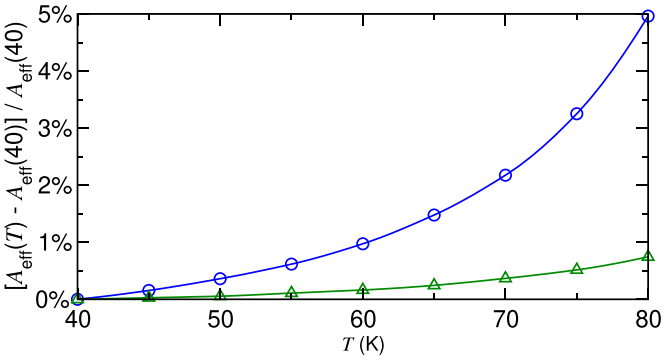

Figure 13. The fractional change in $A_{\rm eff}(T)$: —— 0.6 for the loop in figure 6(a); —— 0.6 for the loop in figure 5.

engineering) developed in the early 1970s for semiconductor circuit simulation. This evolved in the early 1980s into SPICE2. Around then the Berkeley Cryoelectronics Group developed JSPICE, by adding Josephson junctions to SPICE2. [62] SPICE2 and hence JSPICE had some limitations, and a much improved and widely-accepted version, SPICE3, appeared in 1989. Whiteley [63] added Josephson junctions soon after to make his custom version, JSPICE3. Whiteley subsequently developed a successor to JSPICE3, as part of a package of tools called XicTools for schematic capture and mask design. The circuit simulator in this package is `WRspice` and until recently it was a commercial licensed product, but it is now available free-of-charge for a wide range of platforms [29].

`WRspice` is a powerful and versatile simulator, with built-in graphics display for output, and a wide range of functionality that can be included in the input circuit file, for example loops with variable substitution, or post-processing operations like averaging, Fourier transforms, etc. For all of its capabilities see the `WRspice` User's Guide [29].

5.2. `JSIM`

`JSIM` also originated in Berkeley, in 1989, but not directly from the SPICE source code tree. Instead it was developed for a specific project by Fang *et al* [64, 65] and uses a different numerical method that was much faster than the SPICE code at that time. It is intended just for superconductor simulation and has a limited range of component models: the usual passive components, including a transmission line, DC, AC and piecewise voltage and current sources and a junction model. It does only transient analysis. The circuit file syntax and the junction model are almost exactly the same as those for `WRspice`, though data output formats differ. Despite its age it remains a popular simulator, though it has no graphical interface and no post-processing capabilities; users must add those. For many circuits it is still faster than `WRspice`, especially for ones where all nodes are in the voltage state. For the very many comparisons this author has made for simulations of analogue devices at 77 K, it gives identical results to `WRspice`.

In the 1990's Satchell added thermal noise sources to the original `JSIM` code [66], which can be added by a script as current sources in parallel with the $R_{\rm nj}$'s for each junction, making it an ideal simulator for HTS devices.

5.3. *JoSIM*

JoSIM is a recent and ongoing development by Delport *et al* [67] that aims to replace `JSIM` and to give greater simulation speeds for circuits with large numbers of junctions. It uses the same SPICE-like syntax as `JSIM`. Linux and Windows version are available [68]. From [67] it appears that the speed advantage of JoSIM over `JSIM` is modest for circuits with less than a few hundred junctions. It is designed to be expandable and customisable—planned additions include noise sources and a Werthamer [9] junction model.

5.4. *JOINUS*

JOINUS (Josephson Interface Utility Software) [69] is a recent graphical front-end that uses either `JSIM`, JoSIM or `WRspice` to simulate analogue or digital circuits and to plot results graphically. The motivation and emphasis is to support the future development of complex digital circuity with large junction counts [40].

5.5. *PSCAN2*

This program [70] is a dedicated superconductor simulator with a strong emphasis on the design of LTS RSFQ circuits. It has evolved from earlier versions (PSCAN [71] and PSCAN96 [72]) developed by Polonsky *et al*. It makes extensive use of Python modules for both the main program and the graphical interface. Modules can also be used for post-processing, for example to generate $I-V$ curves. Unlike `WRspice` and `JSIM`, it includes a Werthamer [9] model. PSCAN2 does not have noise sources built in, which is a drawback for HTS device modelling, though it appears it is possible for the user to add noise sources externally, with some effort [73, 74]. It seems not to be widely used, perhaps due to the large number of Python modules and the limited documentation.

5.6. *PySQIF*

This is a recent Python-based front-end and post-processing package [75] that uses `WRspice` at its core. Its developers target it mainly at Bi-SQUID simulation but is applicable to any Josephson device. Bi-SQUIDs were introduced by Kornev *et al* [76] and potentially can linearize the voltage response of a SQUID to applied flux.

5.7. *Verilog-A models*

Some commercial simulators have features that are highly attractive for Josephson circuit simulation, but are intended for semiconductor simulation only and do not have a built-in Josephson junction model. A model can be added to some such simulators by a Verilog-A file. This is an industry-standard approach [77]. A simple Verilog-A file for a junction is at

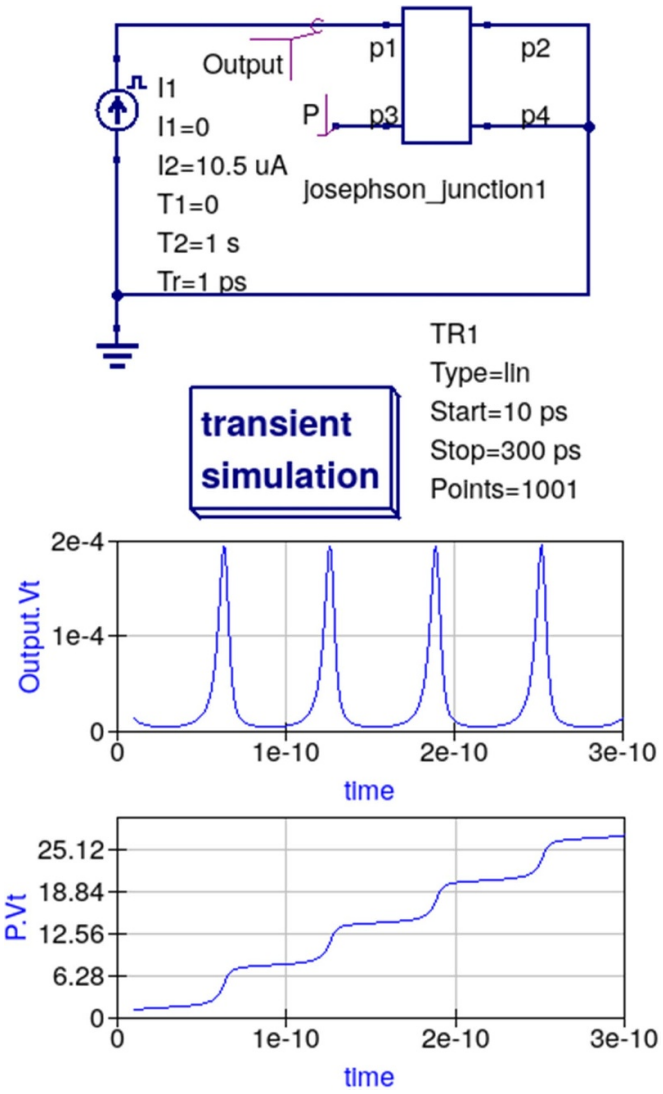

Figure 14. Transient simulation by Qucs of a single junction.

[29, 78] has a more complex one, intended for analogue and digital devices. Appendix C has more technical details.

An example is the use of the advanced development system (ADS) from Keysight Technologies [79]. This powerful package can be used to design RF and microwave thin-film devices, and it has been used very effectively to model HTS Josephson mixers, [80, 81] by adding the Verilog-A model from [78]. This model can also be added to the shareware simulator Qucs [82]; figure 14 shows a simple example. Qucs also has some modest microwave design capabilities. Other semiconductor simulators with Verilog-A capabilities include the full licensed versions of SIMetrix [83] and TINA [84].

It is also possible to replicate the Verilog model in any SPICE-like simulator, without recourse to Verilog, since equations (1), (2) and (5) can be simulated using a voltage-dependent current source. An example is in [85], page 108.

5.8. Adding noise sources to `JSIM` and `WRspice`

`WRspice` and `JSIM` add noise internally in somewhat different manners. For both, a noise current source is added in parallel with each junction shunt resistor, so for example a noise source `iR1` is added to a resistor `R1`.

`WRspice` uses its internal `gauss` function to define a noise source in the header of the circuit file, [86, 87]:

```
*@ define noise(r,t,dt,n)\
gauss(sqrt(2*boltz*t/(r*dt)), 0, dt, n)
```

where `r` is the resistance and `t` is the temperature. `dt` is the so-called lattice time increment—the inherent bandwidth is one half of 1/`dt`, as per Nyquist; `n` is the interpolation method, 0 or 1. [86] Then for example if `R1` is 5.0 Ω and is connected between nodes 7 and 0, noise is then added like so:

```
R1 7 0 5.0
iR1 7 0 noise(5.0, 77, 0.5p, 0)
```

`JSIM` has an internally-defined noise source [66] and uses this code

```
R1 7 0 5.00
iR1 7 0 NOISE(29.2pA 0.0p 1.0ps)
```

where the 29.2pA is the noise current per root Hz at 77 K, for the resistance in the preceding line and the 1.0ps is similar to `WRspice`'s lattice time increment. Scripts are available for `JSIM` to add noise sources to all resistors, except those named like `Rz`..., where the 'z' indicates that noise should not be added—for example one of a network of resistors for distributing bias current uniformly to a SQIF row as will be seen later in figure 19(a).

Owing to the way in which noise is added to `JSIM`, at high temperatures a statistically rare noise transient can cause its solving routines to fail to track correctly across one timestep, causing `JSIM` to trap the error and halt. Such events are very rare and can be detected easily and the simulation re-run. There is a detailed technical comparison in [87] about noise in `WRspice` and `JSIM`.

6. Post-processing

6.1. Inductance

`FastHenry` generates an impedance matrix Zc.mat, with all the real parts of its elements zero. The routine `MakeLcircuit` supplied with `FastHenry` can be used to extract partial inductances and coupling coefficients, plus a code snippet suitable for `JSIM` or `WRspice`. It has been modified by this author to create a better form of `JSIM` code and also to output an inductance matrix $\mathbf{L}$ that can be imported into Matlab [88] or Octave [89] and manipulated as needed. `3D-MLSI` generates an output file containing a pure inductance matrix $\mathbf{L}$ which can be processed in a similar way.

6.2. Time averages

The simulators output a time-varying voltage $V(t)$ for devices in the voltage state, but $I-V$ (current–voltage) and $V(B)$ (voltage-field) plots need the time-average $\overline{V(t)}$, taken by repetitively running `JSIM` or `WRspice` for each of a sequence of I or B points. At $T=0$ it is straightforward to extract $\overline{V(t)}$

from the phase ϕ using equations (3) and (4), but, with noise added and especially at 77 K, it is better to simply compute $\overline{V(t)}$ from a sequence of $V(t)$ values. For both `WRspice` and `JSIM` a typical transient analysis statement to do this is

```
.tran 1ps 21ns 1ns
```

with data sampled every 1 ps, from 1 ns to 21 ns to generate 2000 data points. This example includes an initial delay of 1 ns, so that data is not output for the 1 ns this particular circuit takes to settle. It is wise to look also at the standard deviation in the average to ensure that enough points are being sampled.

6.3. Data smoothing

$V(B)$ plots for SQUIDs and SQIFs simulated at 77 K can still be noisy even after taking long averages of $V(t)$. To derive $\mathrm{d}V/\mathrm{d}B$ the $V(B)$ data first needs to be smoothed in a manner that does not corrupt its underlying features. O'Haver [90] has a number of useful Matlab/Octave routines for taking moving-averages along noisy data plots and forming the differential from the smoothed data.

6.4. Fourier transforms

Procedures such as getting output spectra from Josephson mixers or the voltage or field spectral densities S_V and S_B for SQUIDs and SQIFs need the Fourier transform of $V(t)$ or its PSD. The Matlab/Octave `pwelch` function is useful for the latter, but care needs to be taken with normalising its output, to allow for the chosen fast fourier transform (FFT) window, and also the coherent-gain and noise-gain factors, as usefully discussed in [91].

7. `FastHenry` models for some small SQUID arrays and SQIFs

First, a general point: self and mutual inductances are defined by closed loops, with ports connected to current sources that generate self and mutual flux. These currents and their fluxes define the inductances; these are entirely a function of the geometry of the parts of the structure—sizes, thicknesses, spacings, current density distribution (controlled by $\lambda(T)$), etc 'It is important to observe that the inductance of a piece of wire not forming a closed loop has no meaning.' ([31], from Weber).

But a structure like a small SQUID array or SQIF can be broken into parts using the PEEC concept [31] in a way that allows junctions and current biases to be incorporated subsequently in a physically-valid manner. `FastHenry` extracts the *partial* inductance of all N_s 2-port segments and generates an $N_\mathrm{s} \times N_\mathrm{s}$ inductance matrix $\mathbf{L}$; section 7.1 expands on this. The elements L_{ij} with $i = j$ are the partial self inductances and the off-diagonals with $i \neq j$ are mutual inductances.

The L_{ij} are then assembled into a simulation circuit as a set of self inductances $L_i = L_{ii}$ $(1 < i < N)$ and coupling coefficients $k_{ij} = L_{ij}/\sqrt{L_{ii}L_{jj}}$. Then junctions, plus sources for bias current and magnetic field are added, and the code is fed to `JSIM` or `WRspice`. The procedure must connect all partial self inductances into closed loops. The order in which parts are wired together must be consistent between the physical layout and the circuit file (the ● notation for inductors is a useful aid). Mutual inductance must be treated as a *signed* quantity, since both `FastHenry` and `3D-MLSI` do this, so the k_{ij} are signed (unlike treatments by others that arbitrarily declare M to be always positive).

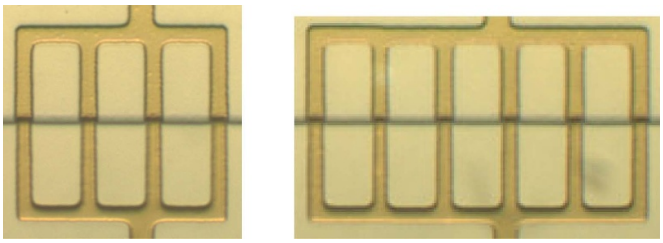

(a) 4 junctions. **(b)** 6 junctions.

Figure 15. Small arrays with step-edge junctions along the centre line. Each loop is $20\,\mu\mathrm{m} \times 6\,\mu\mathrm{m}$ on the inside and the tracks are $2\,\mu\mathrm{m}$ wide. These are similar to the arrays in [92], but with equal-area loops.

7.1. Small SQUID arrays—equal-area loops

Figure 15 shows two small, narrow-track arrays from a set fabricated by CSIRO.

`FastHenry` will generate realistic models of arrays like this, since the $2\,\mu\mathrm{m}$ track width is small compared to the loop dimensions. As an example figure 15(a) is broken down into six inductors, as in figure 16 (plus a seventh, not shown, a long distant strip that generates an approximately-uniform field). `FastHenry` generates a 7×7 inductance matrix from which the `JSIM` file is created, see appendix D. This can then be run through `JSIM` and post-processed to create *e.g.* the $V(B)$ plot in figure 17.

This simulation can be compared for verification with the theoretical analysis by Oppenländer *et al* [3] of arrays like this with n junctions (or $n-1$ loops), who were restricted to the limit $\beta \to 0$ (so they included no mutual coupling between loops). They derived the voltage as a function of the flux Φ_L in one loop:

$$v = \frac{V}{I_\mathrm{cj} R_\mathrm{j}} = \sqrt{J_\mathrm{n}^2 - \left[\frac{\sin\left(\pi \dfrac{n\Phi_\mathrm{L}}{\Phi_0}\right)}{n \sin\left(\pi \dfrac{\Phi_\mathrm{L}}{\Phi_0}\right)}\right]^2} \qquad (12)$$

where $J_n = I/(nI_\mathrm{cj})$. Their analytical result for $n = 4$ and $\beta = 0$ very closely matches the $\beta = 0.035$ simulation in figure 17—so close that they are indistinguishable. For larger values of β the subsidiary minima in the simulated $V(B)$ plot disappear, some asymmetry appears and the plot shifts from $B = 0$; this is due to the inclusion of mutual inductance in the simulation model and also the off-centre bias feed. This simulation was for $T = 0$ to allow comparison with equation (12) from [3]; all other simulations presented in this Review are for $T = 77\,\mathrm{K}$.

From the main period B_0 in figure 17 the simulated $A_\mathrm{eff} = B_0/\Phi_0 = 176.3\,\mu\mathrm{m}^2$. The expected value for this narrow-track loop is $22 \times 8 = 176\,\mu\mathrm{m}^2$ (see section 4.5) and the

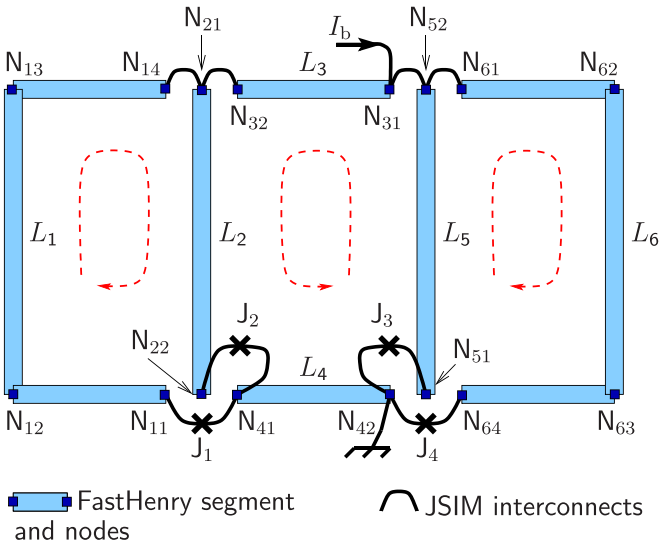

Figure 16. A PEEC model of the 4-junction array in figure 15(a), shown in exploded form for clarity. The partial inductances extracted from `FastHenry` are wired into closed loops, either directly or via junctions as shown, by connections within the `JSIM` input file. The red dashed lines define the connection order for the parts of the three loops. Spatially co-located segment terminal nodes are (N11, N22, N41), (N14, N32, N21), (N31, N52, N61) and (N42, N51, N64). The bias current I_b is fed in at node N31 and out at N42, *i.e.* directly above and below junction J_3. The true feed points are slightly to the left of these, as in figure 15(a). The effect is negligible.

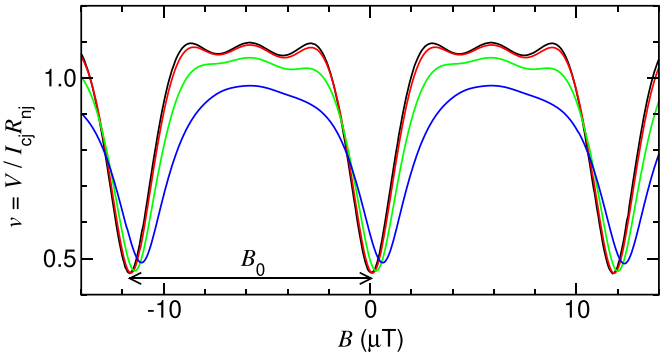

Figure 17. Simulated $V(B)$ curves at $T = 0$ for the figure 15(a) array, for $\beta = 0.035, 0.071, 0.18$ and 0.35, (and). The field B was generated in this model by a Helmholtz coil.

experimentally-measured period for the figure 15(a) device gave $\approx 180\,\mu\text{m}^2$. The agreement between these data is therefore excellent.

7.2. *Small arrays of loops of unequal area*

The methods established to use `FastHenry` and `JSIM` for small arrays with narrow tracks can be extended to any type and size of array, with any bias connection points, like the two small test arrays with loops of unequal areas in [92], shown in figure 18.

As expected their $V(B)$ plots show a range of superimposed periods. There are too few loops and insufficient random

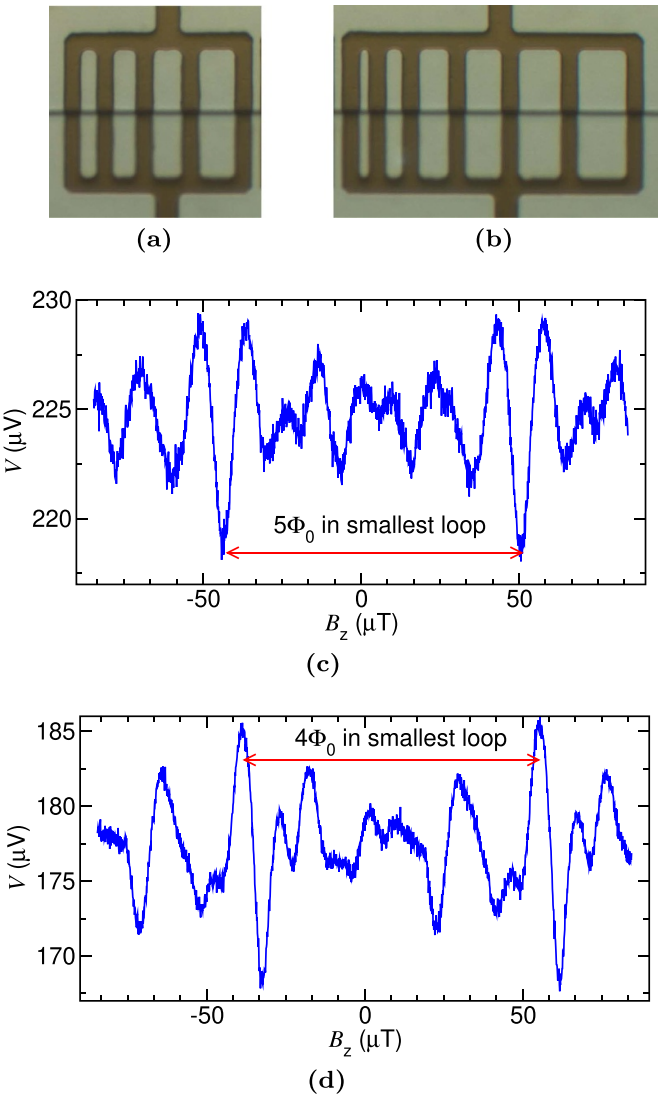

Figure 18. Two small arrays with loops of unequal area. The hole widths for (a) are 3, 4, 5, and 6 μm and for (b) they are 2, 3, 5, 6, 7 and 8 μm. Track widths are 2 μm. $V(B)$ curves in (c) and (d) are for arrays (a) and (b) respectively. Simulation was at $T = 77$ K.

variation in loop areas to show true SQIF responses. Fourier analysis (not reported here) identifies periods in B corresponding to the area of each loop. The largest modulation amplitude comes from the smallest loop in each array, as this has the smallest β. All of this has been explored more fully elsewhere [50].

8. Models that require `3D-MLSI`

One of the key remits of the procedures reported in this Review was to model and attempt to understand the experimentally-observed behaviour of large SQIF arrays [93].

In their entirety these large 2D arrays are beyond the capability of inductance extraction by `3D-MLSI`. Part of the issue is that the horizontal rows in these are interconnected vertically by broad tracks or bus-bars. Some insight was gained by first

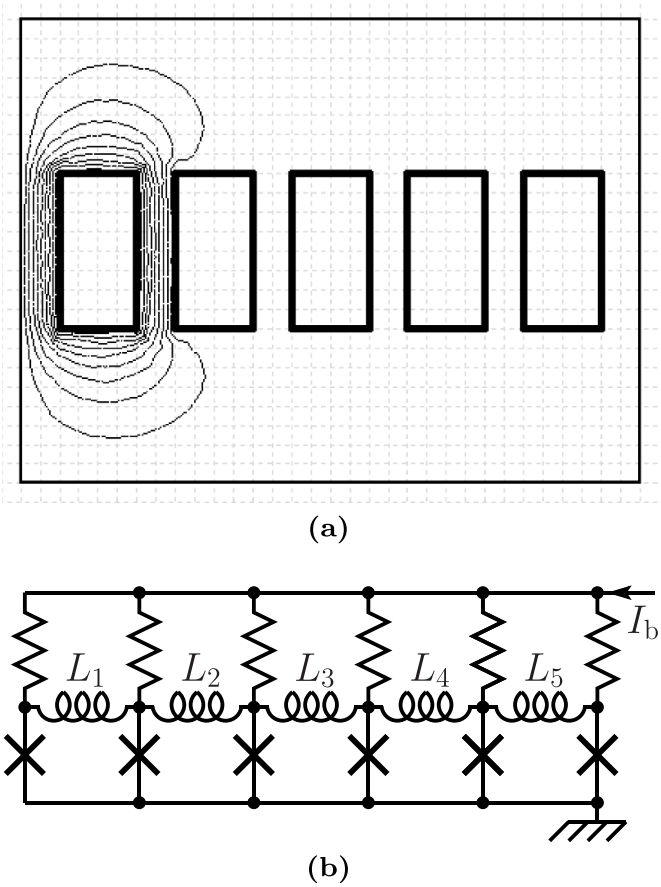

Figure 19. (a) In this 3D-MLSI closed-loop model there are five loops with five self-inductance current paths around them (only one is shown) and no terminals. (b) Its JSIM circuit. Bias current I_b is fed in via six equal noiseless resistors.

looking at small 1D arrays with broad busbars, and then moving to a 1D SQIF with 49 loops—one row of the 20 000 junction SQIF array in [93]. These simpler structures can be analysed with 3D-MLSI.

8.1. Small 1D arrays

8.1.1. A closed-loop 3D-MLSI model. This is the simplest, like the five-loop $N = 5$ example in figure 19(a). The model has no terminals and so is not a true 2-port device and does not fully model a real device. 3D-MLSI extracts the self inductances L_i of each closed loop and all the mutual inductances between them. Note that L_1 and L_5 are found to be larger than the other loop inductances, their A_{eff} are smaller and their mutual coupling to their sole nearest neighbour is less. These *end effects* are due to the different current flow around end loops and their coupling to B_z, as figure 19(a) shows and are common to all arrays and 1D SQIF rows with more than a few loops.

Its equivalent circuit for Josephson simulation, figure 19(b), has L_1 to L_5 in a series chain. Bias is fed via a set of resistors to stop it creating unrealistic flux. The resistors are noiseless. This is flood, or uniform or homogeneous current bias. It seems likely that bias current *does* flow in and out uniformly like this in most rows within a 2D SQIF array. Note that some of the earliest designs of SQIF [94] had built-in thin-film resistors to achieve uniform bias just like this.

This closed-loop model is *extendable*. Arrays and SQIF rows with broad electrodes with more than 20 or so loops cannot be modelled in one piece with 3D-MLSI, due to the program's memory limitation. However, longer ones can be broken up into overlapping sections, in a manner that accurately preserves mutual coupling and excludes the end effects associated with each sub-section. More details are in appendix E. Each of these are separately processed by 3D-MLSI and then an inductance matrix and equivalent simulation circuit can be assembled for the complete structure. As noted, this will only work correctly for SQIF rows with a *uniform* bias-current feed. It has been used to analyse such rows with $N = 49$, as shown later in section 8.2.

8.1.2. A split-loop model. SQUID arrays with $3 < N < 30$ analysed using the closed-loop model show $V(B)$ responses with periods that closely match experiment, but some extra structure seen in the measured data is *not* reproduced. These arrays have bias terminals, like figure 20(a) and to model a real device the effects of bias current must be included. This needs split-loop models, figure 20(b). The equivalent circuit is then like figure 20(c), which will correctly include all flux created by bias currents. The non-physical resistors in figure 19(b) are no longer needed and it is now a true two-port device.

The split-loop model is not extendable, unlike the closed-loop model. This sets a limit to the largest array that 3D-MLSI can model: SQUID arrays and SQIF rows with up to about $N = 25$ are feasible. 3D-MLSI can only process larger ones with a coarser FEM mesh, which introduces unacceptable errors. Figure 21 shows the layout for an $N = 20$ SQUID array and some streamlines with realistic bias connections, fed by central tracks 8 μm wide. This model does not include any part of the bias tracks themselves; this has been explored [50] but is not reported here.

Figure 22 compares simulation and experiment for this array. The main periods are closely equal and some of the subsidiary peaks between the main ones are reproduced qualitatively. This extra structure disappears if the bias current is fed uniformly (like figure 19) showing it is due to the flux from the bias currents to each junction.

8.2. Large SQIFs

The methods outlined above have been used to simulate 1D SQIF arrays with $n = 49$, representing a row in the 2D arrays labelled A2 and A3 in [93]. A3 has extra-broad busbars, as figure 23 shows. The closed loop model, with uniform bias, has to be used and the arrays are split into fifteen overlapping sub-sections (see section 8.1.1). This generous overlap ensures that end effects of the sub-sections are avoided and that all neighbouring mutual inductances are preserved. Each section runs through 3D-MLSI with an adequately-fine FEM mesh.

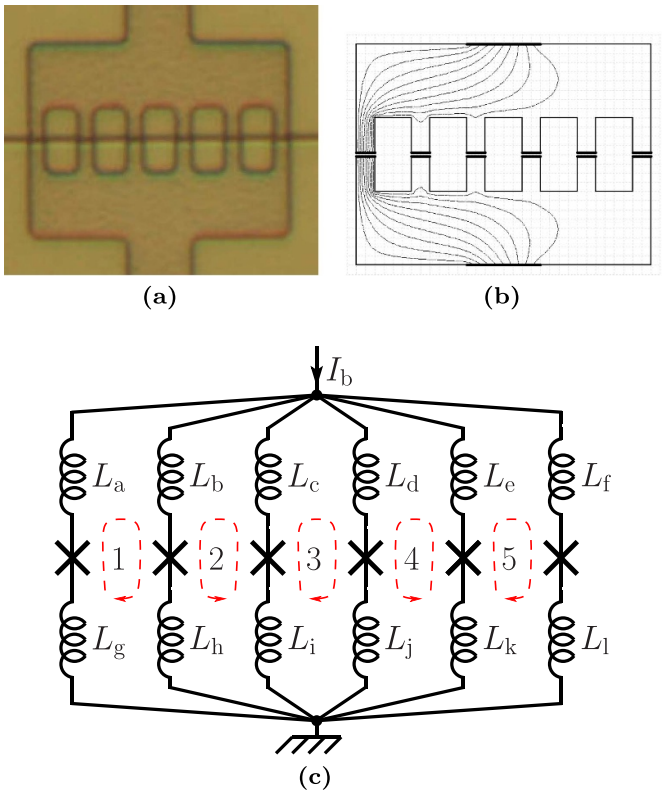

Figure 20. (a) The device (b) the `3D-MLSI` model has gaps with terminals (shown as black bars with their thickness exaggerated for clarity) where junctions will be added. It has two more terminals for bias current (which could be placed anywhere around the edges, with any width). This example shows bias current flow solely through an end junction. (c) `JSIM` simulation circuit.

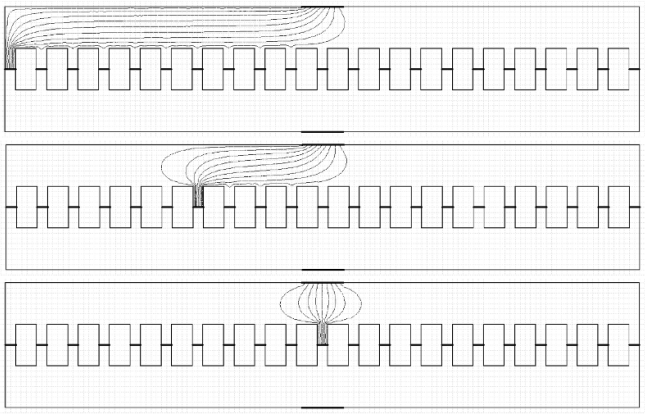

Figure 21. Split-loop `3D-MLSI` model, for an $N = 20$ array. Streamlines are from the top 8 μm-wide terminal to junctions 1, 7 and 11. Streamlines to other junctions are similar. Each streamline represents $1/(n)$ of I_b, if all R_{nj} values are identical.

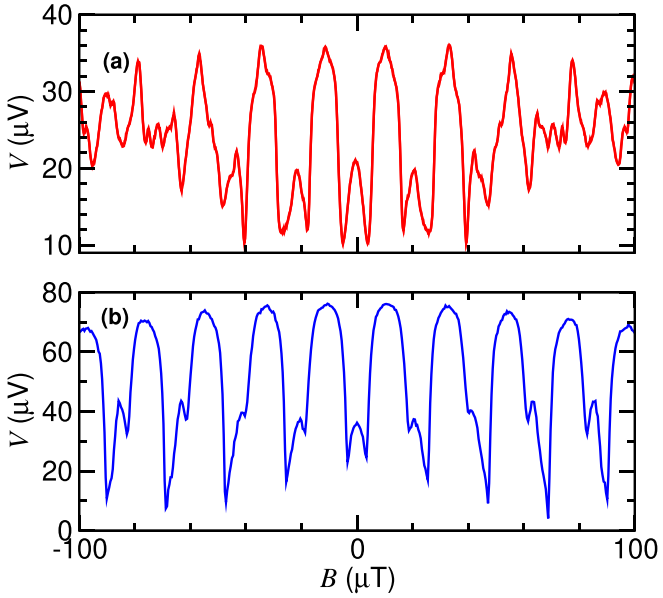

Figure 22. (a) Measured and (b) simulated $V(B)$ plots for the 20-loop array in figure 21.

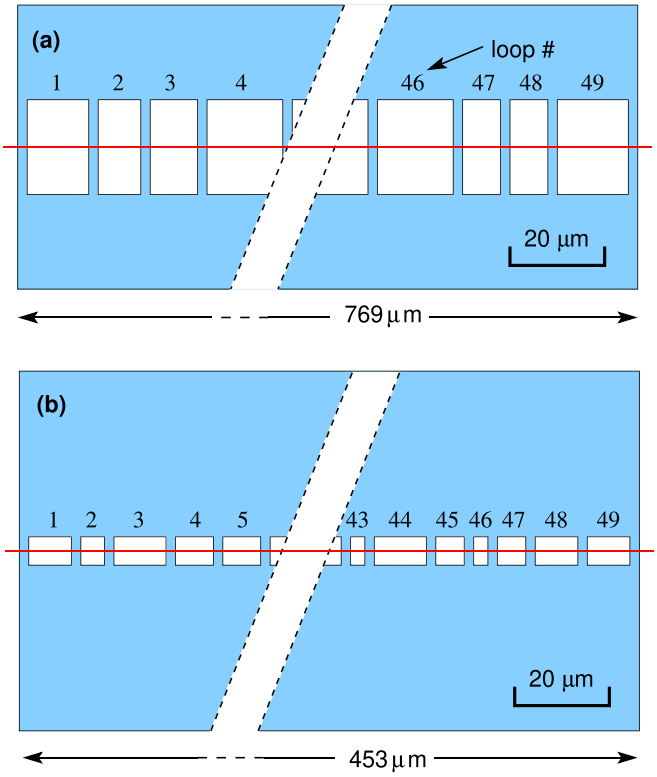

Figure 23. Layout of 1D SQIF rows from 2D arrays, (a) A2 and (b) A3 from [93]. Step-edge junctions are on the red line.

Figure 24 shows (a) the $V(B)$ response for an A2 row with the characteristic SQIF 'anti-peak' and (b) its derivative dV/dB. A SQIF acting as a small-signal field detector would normally be biased by choosing B and I_b to maximise dV/dB. This maximum is related to $\overline{\beta} = 2\overline{L}I_{cj}/\Phi_0$, where the average loop inductance $\overline{L} = 50.4\,\text{pH}$ for the A2 structure. So $\overline{\beta}$ is controlled at the design and fabrication stages by $\overline{L}$ and I_{cj}. Then, I_b needs to be chosen to maximise the maximum value of dV/dB, which has been done for the eight plots in figure 24(b). Figure 25 shows the simulated dependences of $V(B)$ and dV/dB on I_b for an A3 SQIF row which has $\overline{L} = 16\,\text{pH}$. dV/dB attains its maximum value for

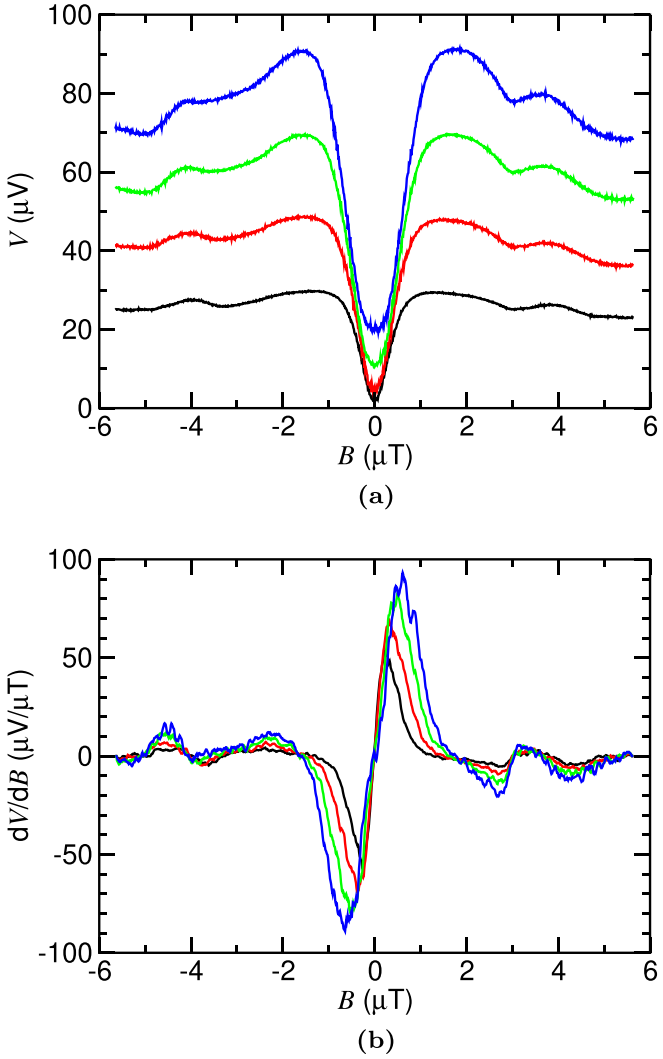

Figure 24. 1D A2 SQIF row at 77 K [93]. (a) Its simulated $V(B)$ curve, showing the characteristic anti-peak, for four values of I_{cj}: 10, 20, 40 and 80 μA, corresponding to $\overline{\beta} = 0.49, 0.98, 1.95$ and 3.90 respectively. (b) dV/dB for this device.

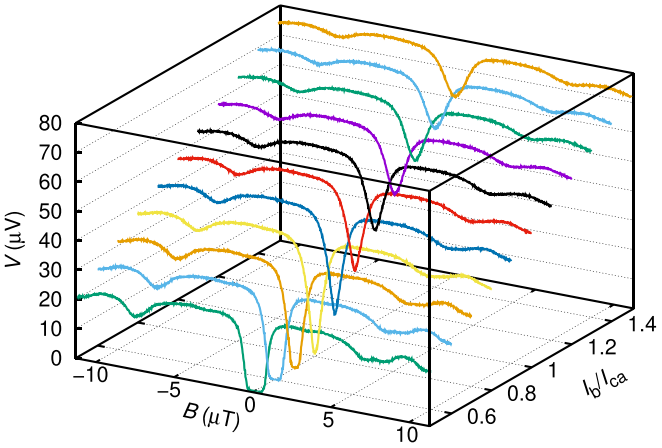

(a) $V(B)$ dependence on array bias current I_b.

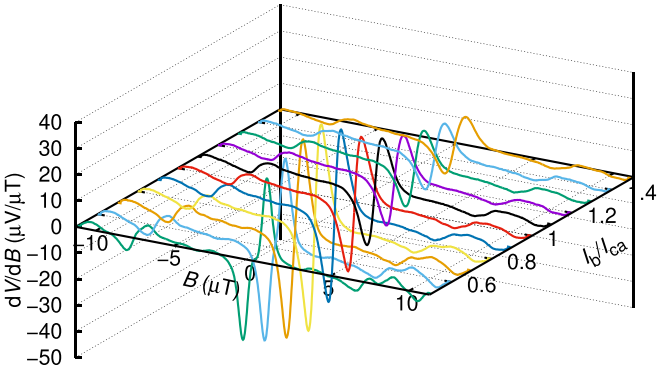

(b) dV/dB derived from figure 25a. The maximum and minimum are for $I_b \approx 0.8 I_{ca}$, either side of $B = 0$.

Figure 25. Simulations of a 49-loop 1-D A3 SQIF row [93] at 77 K, for a range of array bias currents I_b, normalised to the array critical current I_{ca}. $I_{cj} = 10\,\mu$A, $I_{ca} = 500\,\mu$A, $R_{nj} = 5.25\,\Omega$.

$I_b \approx 0.8 I_{ca}$—well below I_{ca}. This is related to the characteristic noise rounding of $I - V$ curves for SQIF rows with many loop and junctions, which will be discussed briefly in section 9.

9. Noise rounding of *I–V* curves in long arrays

Simulation has shown that long SQUID arrays and 1D SQIF arrays both have a characteristic form of their noise-rounded $I - V$ curves. This reaches a limiting shape as the loop number N increases beyond about six at $T = 77$ K. In addition the degree of rounding becomes more pronounced as the average loop inductance increases. This is associated with the parameter L_{th} mentioned in section 2.3. This is a significant effect, as the shape of the $I - V$ strongly influences the value of array bias current that gives the maximum $V(B)$ modulation. Figure 26 illustrates the key points for an array with $1 < N < 31$. The noise rounding is less than for just one junction of the type used in the array, as expected, but is more severe than one single junction with a critical current equal to that of the whole array. Figure 27 shows a similar view of the $I - V$ curves for a SQIF row with 25 junctions.

10. Single-junction mixers

The basic properties of single-junction HTS mixers, such as those made recently by CSIRO [80, 81, 95–107] can be modelled with `JSIM` or `WRspice`. [108] figure 28 shows a basic circuit for mixer simulation. Current sources provide DC bias and RF and LO drive. Figure 29 shows a typical output spectrum. The drawback with this simple model is the lack of isolation between the RF, LO and IF ports, and as a result, all mixing products appear with the IF output. In real devices, matched microwave filters on each port provide isolation between input, LO and output, but in `JSIM` or `WRspice` models it is virtually impossible to replicate such filters. Real devices are also driven by 50 Ω voltage sources, rather than current sources and there is usually a 50 Ω IF termination.

Given these limitations, modelling of HTS mixers has beneficially moved to using the ADS microwave modelling package and a Verilog-A junction model, as discussed in

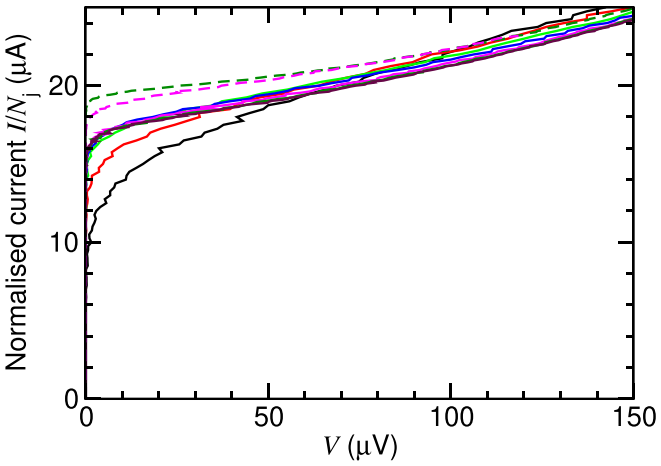

Figure 26. Array $I-V$ curves as a function of junction number n, with current scaled by n. —— $N_j = 1$ with the highest noise rounding, as expected. —— $N_j = 2$. Other superimposed solid curves are for 4, 6, 11, 21 and 31 junctions. $L = 17.6\,\text{pH}$, $I_{cj} = 20\,\mu\text{A}$, $R_{nj} = 10\,\Omega$, $T = 77\,\text{K}$. The dashed curves are for a single large junction equivalent to either 11 (- - -) or 31 (- - -) junctions ($I_{cj} = 220$ or $620\,\mu\text{A}$, respectively), in the limit $L \to 0$.

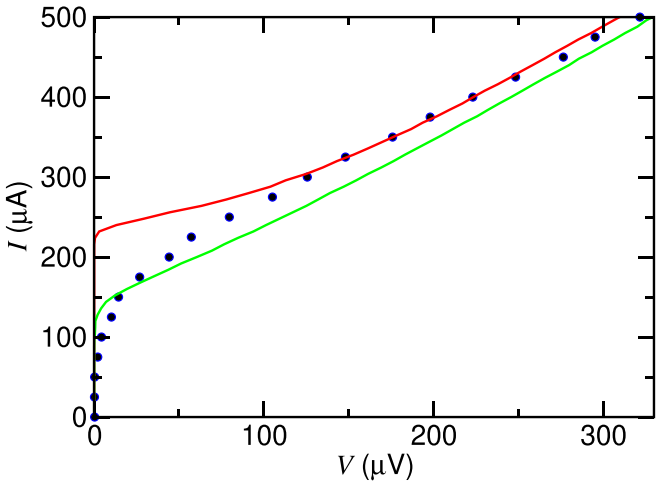

Figure 27. Analysis of $I-V$ curves simulated for a 25-junction SQIF row with $I_{cj} = 10\,\mu\text{A}$, $R_{nj} = 18.7\,\Omega$ and $T = 77\,\text{K}$. ● single junction with I scaled by 25 times; —— single junction, $I_{cj} = 250\,\mu\text{A}$, $R_{nj} = 0.748\,\Omega$; —— 25 junction SQIF row.

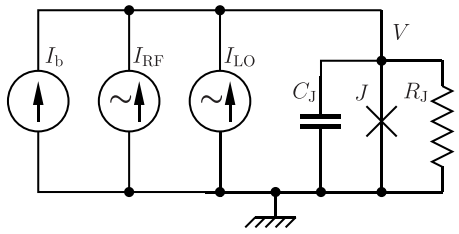

Figure 28. JSIM mixer model. The junction has a DC current source for bias I_b. AC current sources I_{RF} and I_{LO} provide RF and LO inputs.

section 5.7. This work has been developed by Zhang and colleagues at CSIRO [80, 81, 106].

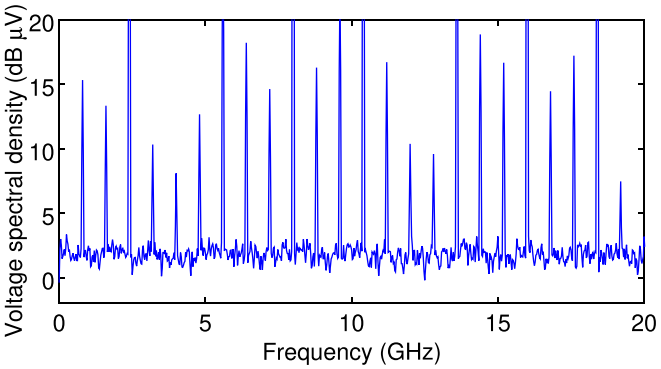

Figure 29. A typical spectrum at 40 K, for $f_{RF} = 10.4\,\text{GHz}$ and $f_{LO} = 8\,\text{GHz}$. Mixing of harmonics of f_{RF} and f_{LO} generates the extra peaks, in addition to $f_{IF} = 2.4\,\text{GHz}$.

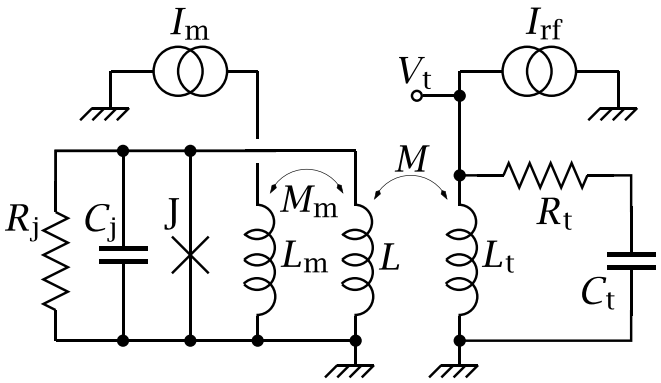

Figure 30. An ideal RF SQUID model. The DC flux Φ to be measured is created from source I_m, with $M_m = \kappa_m\sqrt{L_m L}$.

11. RF SQUIDs

Either `JSIM` or `WRspice` can be used very effectively to model radio-frequency SQUIDs with an equivalent circuit like figure 30. The SQUID has inductance L, plus a single junction J with critical current I_c, a shunt resistance R_j and capacitance C_j. If $\beta_L = (2\pi L I_c)/\Phi_0 > 1$ the SQUID is hysteretic or dissipative, otherwise it is non-hysteretic. It is coupled inductively to a tank circuit formed from L_t and C_t resonant at $\omega_0 \approx 1/\sqrt{L_t C_t}$. The mutual inductance $M = k\sqrt{LL_t}$ with coupling coefficient k. The tank circuit has some resistive loss represented by R_t and a quality factor $Q \approx \omega_0 L_t/R_t$. Current noise sources are added to both R_j and R_t. The tank circuit usually has a high Q and is weakly coupled to the SQUID ($k \ll 1$), to maintain the optimum condition $k^2 Q \approx 1$. The root mean square or RMS output voltage is V_t.

It is driven by a sinusoidal RF current with amplitude I_{rf} at frequency ω. The best flux response is very often when the tank circuit is slightly off-tune, so that $\omega \neq \omega_0$. There may be *no* response when $\omega = \omega_0$ The de-tuning factor δ can be defined [109] as $\delta = 2Q(\omega - \omega_0)\omega_0$.

RF SQUID theory is not trivial and has been treated by several authors [5, 110–112] and others, with a good overview in [5]. Analytical expressions for the tank circuit RF voltage V_t as a function of RF current drive I_{rf} (*i.e.* $I-V$ curves) for RF SQUIDs have been derived independently by Hansma [109],

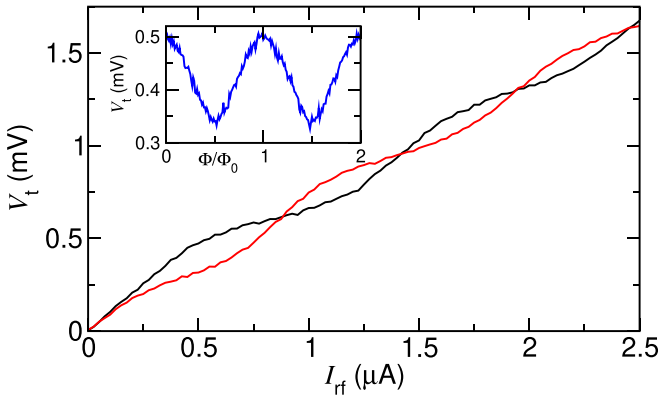

(a) Hysteretic, $\beta_L = 4.56$

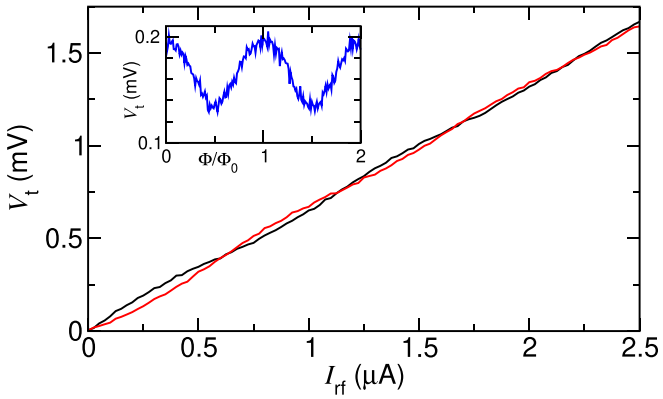

(b) Non-hysteretic, $\beta_L = 0.68$

Figure 31. $V_t(I_{rf})$ plots for a 3 GHz RF SQUID at 40 K. —— $\Phi = 0$, —— $\Phi = 0.5\Phi_0$. The de-tuning parameter $\delta = 1$ which gives the best response. Insets show $V_t(\Phi)$ for I_{rf} giving maximum modulation. Voltages and currents are rms amplitudes.

Chesca [113] and others, and were reviewed by Kleiner *et al* [114]. Simulation provides an alternative to this theoretical approach. As an example, figure 31 shows $V_t(I_{rf})$ and $V_t(\Phi)$ plots for both a hysteretic and a non-hysteretic 3 GHz RF SQUID at 40 K simulated using `JSIM`.

12. Simulation using electronic analogues

In the early days of Josephson technology many authors described electronic analogues of junctions to study their properties. These use room-temperature circuitry to mimic equation (5), with the Josephson frequency equation (4) reduced to typically 1 kHz/volt in the analogue. This makes the junction voltage $V(t)$ readily observable by ordinary laboratory instruments. [115] collates most of the past papers, which are mainly for single-junction analogues, though DC SQUIDs [116, 117] are possible with extra circuitry for loop phase coherence equation (7). Pairs of coupled junctions have also been reported [118].

Electronic analogues are clearly not viable for multi-loop multi-junction devices, but for some situations they still have some merit, potentially for example for single-junction mixers. Simulation is in real time, and the effects of changing temperature, bias or drive frequency are instantly apparent, at the 'turn of a knob'. This can also make them a useful teaching and demonstration tool. With the current availability of low-cost digital modules for synthesis, signal-processing and filtering, it is perhaps worth re-visiting this field.

13. Summary

This Review has shown that freely-available software for inductance extraction and simulation can model fully a variety of thin-film superconducting devices containing Josephson junctions. A quite complex device made up from narrow tracks (with track widths much less than all other dimensions, like figure 15) can use `FastHenry` to extract all self and mutual inductances of its parts with adequate accuracy. But a device with wide tracks or broad areas of superconductor such as figure 20(a) needs `3D-MLSI` to extract its inductances. The effective areas of loops within a device can be also found as part of the inductance extraction process.

The inductive components of the device can then be combined with junction models, passive components, noise sources (to represent Nyquist noise at the chosen temperature) and voltage or current sources in the form of an equivalent circuit. This is then fed to either of two Josephson simulators—`JSIM` or `WRspice`. Both generate results that are distinguishable. In the voltage state `JSIM` generally runs faster than `WRspice`.

Simulations generate a time-varying voltage that needs to be averaged for most analogue devices by post-simulation to create current–voltage characteristics or the variation of terminal voltage with applied field.

Data availability statement

The data that support the findings of this study are available upon reasonable request from the author.

Appendix A. Other inductance extraction procedures

A.1. Induct

This program implements methods developed by Chang [119] for the inductance of two or more superconducting strips of rectangular cross-section and infinite length. It can be used to extract the inductance per unit length of coplanar striplines, as are often used as interconnections or as part of so-called 'linear' HTS DC SQUIDs. It is available as source code from [29].

There must be one conductor or more to act as a return path for current. Like `FastHenry` the method divides conductors into filaments and includes kinetic inductance. Extensive comparisons with `FastHenry` agree well. Each conductor's cross-section is specified by one or more lines in a text input file. Each line has 12 parameters, which in order are: conductor number, (x, y) lower left, (x, y) upper right, penetration depth, x-divisions, y-divisions, x-ratio, y-ratio, x-type, and

y-type. One or more of the conductors must have a number ⩾100 to act as the 'ground' conductor; these must come first. `x ratio`, `y ratio` are similar to the `rw` and `rh` parameters for `FastHenry`. For example, a value of 2 makes adjacent filaments differ in width or height by a factor of 2. `x type`, and `y type` control the organisation of filaments and can be selected to match the expected current distributions; type 0 corresponds to the scheme used by `FastHenry`.

This is a simple example for two parallel co-planar strips 4 μm wide and 0.22 μm thick, with their facing edges 4 μm apart and $\lambda = 0.3\,\mu$m:

```
100 0 0  4 0.22 0.30 13 9 2 2 0 0
  1 8 0 12 0.22 0.30 13 9 2 2 0 0
```

The result for this example is 1.08 pH/μm.

A.2. L-meter

There are references in the literature to this package, much used for inductance extraction for multilayer LTS RSFQ circuits [120]. But it can only be used for structures with a groundplane, so it is not useful for most single-layer HTS devices. The code is available from [121].

Appendix B. Analytical inductance expressions

Formulas rather than inductance extraction can be used for some structures. Some examples are given here.

B.1. Co-planar striplines

Co-planar striplines as shown in figure B1 are commonly used to form so-called linear SQUIDs (*e.g.* [57, 58, 122]) and also as low-inductance interconnects between parts of single-layer devices.

In [123] it is shown that, for unit length, the kinetic inductance L_k and the internal magnetic inductance L_m of a *single*, *isolated* strip of width w and thickness d are given by

$$L_\mathrm{k} = \frac{\mu_0\lambda}{4w}\left[\coth\left(\frac{d}{2\lambda}\right) + \left(\frac{d}{2\lambda}\right)\mathrm{cosec}^2\left(\frac{d}{2\lambda}\right)\right] \qquad \text{(B.1)}$$

and

$$L_\mathrm{m} = \frac{\mu_0\lambda}{4w}\left[\coth\left(\frac{d}{2\lambda}\right) - \left(\frac{d}{2\lambda}\right)\mathrm{cosec}^2\left(\frac{d}{2\lambda}\right)\right]. \qquad \text{(B.2)}$$

This analysis has no restrictions on the relative sizes of w, d and λ.

These free-space expressions can be applied to co-planar lines, providing they are not too close (otherwise the current density distribution across the width of each strip will differ significantly from the case for one isolated strip).

An estimate of the total inductance per unit length is then

$$L_\mathrm{tot} = \mu_0\left[\frac{\lambda}{w}\coth\left(\frac{d}{2\lambda}\right) + \frac{K(k)}{K(k')}\right]. \qquad \text{(B.3)}$$

The second term approximates the inductance contribution from the *external* magnetic field, using the expression for normal-metal coplanar lines at high frequencies where the skin depth is small in comparison with the line dimensions [124]. $K(k)$ is the complete elliptic integral of the first kind, $k = s/(s+2w)$ and $k' = \sqrt{1-k^2}$.

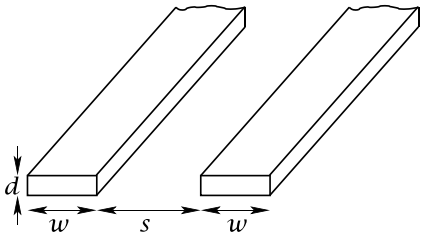

Figure B1. Thin-film co-planar lines.

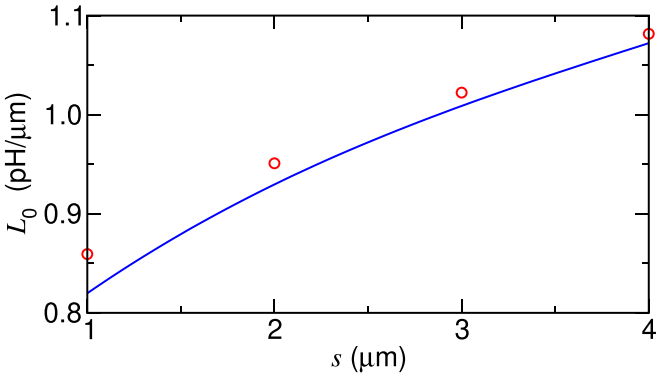

Figure B2. Co-planar stripline inductance estimates for lines like figure B1 with $w = 4\,\mu$m as a function of s. —— equation (B.3); ○ data averaged from `FastHenry`, `3D-MLSI` and `induct`, which differ by no more than 0.2%. End effects for `FastHenry` and `3D-MLSI` have been eliminated to yield true extractions of L_0 for infinitely-long lines.

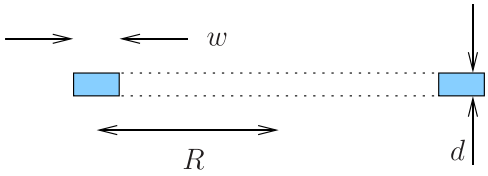

Figure B3. Cross-section of a thin-film annulus.

A test of the validity of equation (B.3) is shown in figure B2, which also includes data derived by `FastHenry`, `3D-MLSI` and `induct`. The latter three all agree well with each other. As expected, for small s the accuracy of equation (B.3) worsens to about 2.5% less than the `FastHenry` value for $s = 1\,\mu$m. Nonetheless equation (B.3) is an acceptable estimate for many situations.

B.2. Planar circular loops

Circular loops or annuli feature in a range of thin-film devices, for example for SQUIDs and circular flux sensing loops. A formula for the inductance L_l of a thin-film annulus, like figure B3, is proposed in [125, 126]:

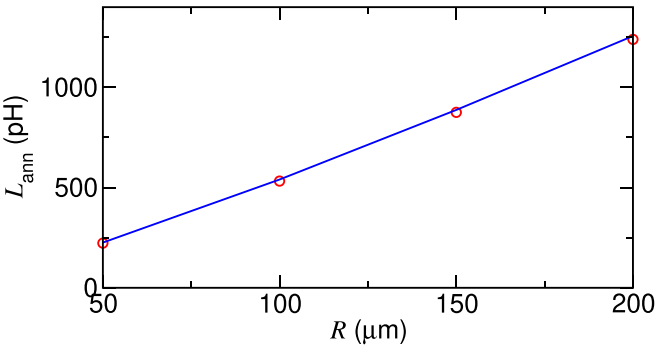

Figure B4. An example comparison of equation (B.4) — with extraction by 3D-MLSI, ○, for $d = 0.22\,\mu$m, $w = 10\,\mu$m and $\lambda = 0.4\,\mu$m.

$$L_1 = \mu_0 R\left[\log_e\left(\frac{8R}{w}\right) - (2 - \log_e 4)\right]. \qquad \text{(B.4)}$$

Its derivation has two limitations: (a) it assumes $\lambda << w$, so the current is localised at edges of the circular track and so there is no contribution included to the inductance from internal magnetic energy. If $w << R$ this error should be small. (b) It does not include kinetic inductance. For these reasons λ and d do not appear in equation (B.4), which is of course unrealistic. The kinetic inductance per unit length will be given by (B.1) so an estimate of the total annulus inductance is

$$L_{=}L_1 + 2\pi R L_{\rm k}. \qquad \text{(B.5)}$$

Formula (B.5) can be tested against inductance extraction. It is difficult to extract annular inductance accurately with FastHenry, but 3D-MLSI can deal with a closed annulus, formed from a circular disk plus a concentric hole. Figure B4 is one example showing good agreement between (B.5) and 3D-MLSI extraction. The agreement holds for a range of annuli with differing dimensions.

B.3. Adapting normal-metal formulas

Various formulas abound in the literature for the self and mutual inductances of normal-metal structures, *e.g.* [127–129] and others. With care some of these formulas can be used to a limited extent for superconducting thin-film equivalents [130], especially when given for normal-metal structures in the high-frequency limit, which makes an approximate equivalence to a superconductor with small λ. But an extra term usually must be added for kinetic inductance.

Appendix C. Verilog-A

A Verilog-A file derived from [78] is listed below.

```
// Copyright 2012 Accellera Systems Initiative
// Licensed under the Apache License, Version 2.0
// (the "License"); you may not use this file
// except in compliance with the License at:
// http://www.apache.org/licenses/LICENSE-2.0

// Minor changes by CMP 17/10/14.
// Added "constants.vams", so can use pi, h and
// e values. Removed localparam statement---not
// supported by admsXml.
// hbar/(2*e) = h/(4*pi*e) = 0.329108e-15, this
// is now defined, so that it does not appear as
// a user parameter. Added "info" & "unit" data.

// Merged orig low & high Tc models into a one;
// increased ranges of values for cj, rj and i0.

// Re-arranged branch contributions, and minor
// change to ddt contributions to be consistent
// with admsXml.

`include "disciplines.vams"
`include "constants.vams"

`define attr(txt) (*txt*)

module josephson_junction (p1, p2, p3, p4);
  inout p1, p2, p3, p4;
  electrical p1, p2, p3, p4;
  parameter real cj = 0.1p from [0.01p:1p]
    `attr(info = "junction capacitance" unit = "F");
  parameter real rj = 10 from (0.1:50)
    `attr(info = "junction resistance" unit = "ohm");
  parameter real i0 = 10u from (1u:2000u)
    `attr(info = "critical current" unit = "A");
  real c1;
  analog begin
  @(initial_step) begin
      c1 = `P_H/(4.0*`M_PI*`P_Q);

  end
  I(p1,p2) <+ ddt(cj * V(p1,p2));
  I(p1,p2) <+ V(p1,p2) / rj;
  I(p1,p2) <+ i0 * sin(V(p3,p4));
  I(p3,p4) <+ ddt(c1*V(p3,p4));
  I(p3,p4) <+ -V(p1,p2);
  end

endmodule
```

A form of the Josephson equations (1), (2) and (5) can be identified in the 'analog begin' block. Because superconducting phase is not an electrical variable, is represented as a voltage (1 V≡ 1 rad) and it appears at an extra terminal p3, see figure 14. Current noise in the junction shunt can be added by omitting the parameter rj in the Verilog-A file and adding a shunt resistor and enabling thermal current noise in the simulator for that resistor. Note also that simulations are for the time-domain only.

Appendix D. PEEC example: a three-loop array

The PEEC method for small arrays and SQIFs with narrow tracks can be illustrated using the 3-loop array in figure 16 as an example. This is split into six tracks plus an extra distant track used to generate a field (and to estimate the effective areas, section 4.5). FastHenry generates a 7×7 inductance matrix $\mathbf{L} =$

$$\begin{array}{rrrrrrr} 27.67 & -4.58 & -0.77 & -0.77 & 2.71 & -1.55 & 0.53 \\ -4.58 & 18.11 & 0.00 & 0.00 & -4.58 & 2.71 & 0.00 \\ -0.77 & -0.00 & 5.06 & -0.29 & 0.00 & -0.77 & -0.27 \\ -0.77 & -0.00 & -0.29 & 5.06 & 0.00 & -0.77 & -0.26 \\ 2.71 & -4.58 & 0.00 & 0.00 & 18.11 & -4.58 & 0.00 \\ -1.55 & 2.72 & -0.77 & -0.77 & -4.58 & 27.66 & 0.53 \\ 0.49 & 0.00 & -0.24 & -0.24 & 0.00 & 0.49 & 466.4 \end{array} . \tag{D.1}$$

The individual loop self inductances can be extracted from the inductance matrix:

$$L_{\text{loop1}} = \sum_{i=1}^{2}\sum_{j=1}^{2} L_{ij} = 36.62\,\text{pH}$$

$$L_{\text{loop2}} = \sum_{i=2}^{5}\sum_{j=2}^{5} L_{ij} = 36.61\,\text{pH}$$

$$L_{\text{loop3}} = \sum_{i=5}^{6}\sum_{j=5}^{6} L_{ij} = 36.62\,\text{pH}$$

all of which equal the inductance of a single isolated loop of the same dimensions.

The elements L_{ij} with $i = j$ are partial self inductances and the off-diagonals with $i \neq j$ are mutuals, with coupling coefficients $k_{ij} = L_{ij}/\sqrt{L_{ii}L_{jj}}$.

The elements L_{i7} or L_{7j} in this example are the mutual inductances to the field-generator (self inductance L_{77}), in this case a single track with a calculated $\alpha = 0.002895\,\text{TA}^{-1}$. The mutual inductances between each loop and this track are

$$M_{\text{loop1}} = \sum_{j=1}^{2} L_{7j} = 0.49\text{pH}$$

$$M_{\text{loop2}} = \sum_{j=2}^{5} L_{7j} = -0.48\text{pH}$$

$$M_{\text{loop3}} = \sum_{j=5}^{6} L_{7j} = 0.49\text{pH}.$$

The effective area A_{eff} of each loop is then

$$A_{\text{eff}} = M_{\text{loop}n}/\alpha \approx 175\,\mu\text{m}^2.$$

The L_{ii} and k_{ij} can be extracted from $\mathbf{L}$ using the `MakeLcircuit` program supplied with the `FastHenry` code, though this author uses a customised version of that. This generates code for `JSIM`:

```
L_1 1 2 27.6647p
L_2 3 4 18.1092p
L_3 5 6 5.0616p
L_4 7 8 5.0616p
L_5 9 10 18.1092p
L_6 11 12 27.6647p
L_track 13 14 466.437p
K_2_1~L_2~L_1 -0.204581
K_3_1~L_3~L_1 -0.06491
K_4_1~L_4~L_1 -0.06491
K_4_3~L_4~L_3 -0.0569496
K_5_1~L_5~L_1 0.121295
K_5_2~L_5~L_2 -0.252712
K_6_1~L_6~L_1 -0.0558763
K_6_2~L_6~L_2 0.121295
K_6_3~L_6~L_3 -0.0649108
K_6_4~L_6~L_4 -0.0649108
K_6_5~L_6~L_5 -0.204581
K_track_1~L_track L_1 0.00449969
K_track_3~L_track L_3 -0.00529398
K_track_4~L_track L_4 -0.00523683
K_track_6~L_track L_6 0.00449061.
```

The inductances must be re-numbered and junctions added, to match the true device layout. The procedures (a) writing the text input for `FastHenry`, (b) running `FastHenry`, (c) extracting inductances and k values from $\mathbf{L}$ and (d) assembling these into a circuit file for `JSIM` or `WRspice` are tedious and error-prone for all but the simplest structures. Instead, it is automated by a custom C program which reads a simple parameter file specifying all key features of the array or SQIF layout, plus junction properties and runs procedures (1)–(4) in sequence, with a wealth of error checks. There are options to feed bias current at any user-defined single point (as in figure 16), or to feed current through a comb of noiseless resistors, that ensures a uniform or 'flood' feed of bias, as was done for some of the first Nb SQIFs [131] to avoid self-field effects.

Appendix E. `3D-MLSI` models for long SQIF rows

Long SQUID arrays (like figure 20 but with $N > 30$) or SQIF rows, as in the A2 and A3 20k arrays in figure 23, with 49 loops and broad bus-bars, cannot be easily modelled by `3D-MLSI`, owing to unavoidable memory and speed constraints. Alternative approaches are needed. The 1D row is split into m smaller sections and inductance matrices $\boldsymbol{L_m}$ are separately extracted by `3D-MLSI` for each. These are then merged into a single sparse matrix $\boldsymbol{L}$ which is used to get the inductances and couplings needed for `JSIM`.

Each of the m sections must be small enough to allow a reasonable value of the parameter `ah` to be used. `ah` sets the FEM mesh size and if too big the `3D-MLSI` solutions are inaccurate. If it is unnecessarily too small, the mesh is too fine and memory limits may be exceeded.

The complete row has to be split into overlapping sections, to avoid unwanted end effects (section 8.1 and figure 19). The exampleUltiMaker-Cura-5.2.2-linux-modern.AppImage to follow attempts to explain this for a 49-loop SQUID array or 1D SQIF row. It is split into $m = 15$ parts, each containing seven loops. A structure of this size will run through `3D-MLSI` with ah $= 1.0\,\mu$m, a value that gives acceptable results. `3D-MLSI` is run in parallel across 15 CPU cores on the 15 parts to generate a set of inductance matrices $\boldsymbol{L_1}$–$\boldsymbol{L_{15}}$. The procedure only needs to be run once, unless the layout or `3D-MLSI` parameters are changed

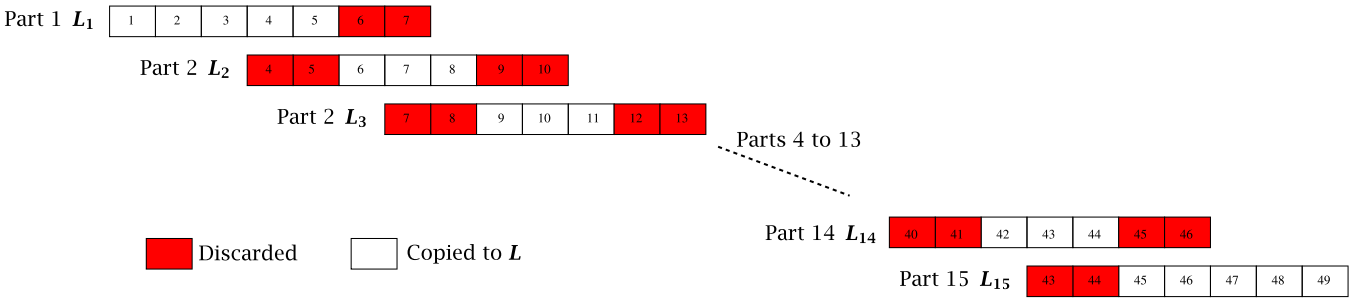

Figure E1. Constructing $\boldsymbol{L}$ from $\boldsymbol{L_1}$ to $\boldsymbol{L_{15}}$ to avoid unwanted end-effects. For simplicity, loops are shown with all the same sizes. The number within each loop is the index n for the loop number in the complete array, $1 \leqslant n \leqslant 49$.

A single inductance matrix $\boldsymbol{L}$ is then assembled from the individual matrices $\boldsymbol{L_1}$–$\boldsymbol{L_{15}}$ in the following manner, which *preserves* end effects at the two ends of the whole array, but *avoids* artificial end effects for the other 13 parts. Figure E1 depicts this procedure.

The columns in each $\boldsymbol{L_m}$ contain the self inductance for a loop, and its mutual inductance to its seven nearest neighbours (mutuals beyond the nearest and next-nearest neighbours are negligible). The first five columns of $\boldsymbol{L_1}$ are copied into $\boldsymbol{L}$, corresponding to loops 1–5 in the complete row. Columns 6 and 7 in $\boldsymbol{L_1}$ are not used, to avoid end effects. Similarly, the last five columns in $\boldsymbol{L_{15}}$ are copied into $\boldsymbol{L}$, but columns 1 and 2 in $\boldsymbol{L_{15}}$ are discarded. For the remaining $\boldsymbol{L_2}$–$\boldsymbol{L_{14}}$, only the central columns 3, 4 and 5 are copied into $\boldsymbol{L}$; the first two and last two columns are discarded, again to avoid end effects. This creates a square matrix of size $5+5+(3\times 13)=49$ in $\boldsymbol{L}$.

There may appear to be a lot of duplication in this method: the structure may seem over-fragmented, and many loops have their inductance extracted twice. But this process ensures all the L_n are in the correct location for `3D-MLSI` to calculate an accurate value of self inductance: L_1 and L_{49} **are** end loops, and they are treated as such; L_2–L_{48} are taken from locations in parts 1–15 where they are **not** at either end of the sub-part. The process also correctly preserves nearest and next-nearest neighbour mutual inductances without end-effect errors.

Finally, cells in $\boldsymbol{L_m}$ for the mutual coupling to the field-generating strip are transcribed into $\boldsymbol{L}$, again not using ones that would have end-effect errors. The resulting 50×50 sparse matrix contains self inductances L_n, plus mutual inductances $M_{n,n+1}$ and $M_{n,n+2}$ between nearest and next-nearest neighbours respectively, and $M_{\mathrm{f},n}$, the mutual coupling between loop n and the field-generating strip. The self inductance of this strip, L_f, is copied from $\boldsymbol{L_1}(7,7)$ into $\boldsymbol{L}(50,50)$ (it has the same value in all the $\boldsymbol{L_m}$).

$\boldsymbol{L}$ can now be processed by matrix software to get sets of self inductances L_1–L_{49} and coupling coefficients $k_{n,n+1}$ and $k_{n,n+2}$ where

$$M_{n,n+1} = k_{n,n+1}\sqrt{L_n L_{n+1}} \tag{E.1}$$

$$M_{n,n+2} = k_{n,n+2}\sqrt{L_n L_{n+2}}. \tag{E.2}$$

Optionally, the $k_{n,n+1}$ and $k_{n,n+2}$ can be omitted, to explore the effects of mutual coupling. The coupling coefficients $k_{n,\mathrm{f}}$ for the coupling of each loop to the field-generating inductance L_f are also included, where

$$M_{n,\mathrm{f}} = k_n\sqrt{L_n L_\mathrm{f}}. \tag{E.3}$$

ORCID iD

Colin Pegrum https://orcid.org/0000-0003-1758-7920

References

[1] J Clarke and A I Braginski (eds) 2006 *The SQUID Handbook: Fundamentals and Technology of SQUIDs and SQUID Systems* vol 1 (Weinheim: Wiley-VCH)
[2] Fagaly R L 2016 *Superconducting Quantum Interference Devices (SQUIDs)* (Wiley, Inc.) pp 1–15
[3] Oppenländer J, Häussler C and Schopohl N 2001 Non-Φ_0-periodic macroscopic quantum interference in one-dimensional parallel Josephson junction arrays with unconventional grating structure *Phys. Rev.* B **63** 024511
[4] Schmelz M, Hopf M, Zakosarenko V, Schönau T, Chwala A, Anders S, Kunert J and Stolz R 2021 Magnetic background field-tolerant SQIF-based current sensors *Supercond. Sci. Technol.* **34** 045015
[5] Koelle D, Kleiner R, Ludwig F, Dantsker E and Clarke J 1999 High-transition-temperature superconducting quantum interference devices *Rev. Mod. Phys.* **71** 631–86
[6] Fagaly R L 2006 Superconducting quantum interference device instruments and applications *Rev. Sci. Instrum.* **77** 101101
[7] Josephson B D 1962 Possible new effects in superconductive tunnelling *Phys. Lett.* **1** 251–3
[8] Josephson B D 1965 Supercurrents through barriers *Adv. Phys.* **14** 419–51
[9] Werthamer N R 1966 Nonlinear self-coupling of Josephson radiation in superconducting tunnel junctions *Phys. Rev.* **147** 255–63
[10] Gulevich D R, Koshelets V P and Kusmartsev F V 2017 Josephson flux-flow oscillator: the microscopic tunneling approach *Phys. Rev.* B **96** 024515
[11] Stewart W C 1968 Current-voltage characteristics of Josephson junctions *Appl. Phys. Lett.* **12** 277–80
[12] McCumber D E 1968 Effect of ac impedance on dc voltage-current characteristics of superconductor weak-link junctions *J. Appl. Phys.* **39** 3113–18
[13] Mitchell E E and Foley C P 2010 YBCO step-edge junctions with high $I_\mathrm{c}R_\mathrm{n}$ *Supercond. Sci. Technol.* **23** 065007
[14] Zimmerman J E and Silver A H 1966 Macroscopic quantum interference effects through superconducting point contacts *Phys. Rev.* **141** 367–75

[15] Tesche C D and Clarke J 1977 dc SQUID: noise and optimization *J. Low Temp. Phys.* **29** 301–31
[16] Clarke J, Goubau W M and Ketchen M B 1976 Tunnel junction dc SQUID: fabrication, operation and performance *J. Low Temp. Phys.* **25** 99–144
[17] Ambegaokar V and Halperin B I 1969 Voltage due to thermal noise in the dc Josephson effect *Phys. Rev. Lett.* **22** 1364–6
[18] Colclough M S 2000 Efficient calculation of the current-voltage characteristic of a resistively shunted Josephson junction *J. Appl. Phys.* **88** 3085–6
[19] Enpuku K, Shimomura Y and Kisu T 1993 Effect of thermal noise on the characteristics of a high-T_c superconducting quantum interference device *J. Appl. Phys.* **73** 7929–34
[20] Likharev K K 1986 *Dynamics of Josephson Junctions and Circuits* (London: Gordon and Breach)
[21] Chesca B 1998 Analytical theory of DC SQUIDs operating in the presence of thermal fluctuations *J. Low Temp. Phys.* **111** 165–96
[22] Chesca B 1999 The effect of thermal noise on the operation of DC SQUIDs at 77K—a fundamental analytical approach *IEEE Trans. Appl. Supercond.* **9** 2955–60
[23] Tesche C D and Clarke J 1979 dc SQUID: current noise *J. Low Temp. Phys.* **37** 397–403
[24] Enpuku K, Tokita G and Maruo T 1994 Inductance dependence of noise properties of a high-T_c dc superconducting quantum interference device *J. Appl. Phys.* **76** 8180–5
[25] Müller K H and Mitchell E E 2021 Theoretical model for parallel SQUID arrays with fluxoid focusing *Phys. Rev.* B **103** 054509
[26] Kamon M, Tsuk M J and White J K 1994 FASTHENRY: a multipole-accelerated 3-D inductance extraction program *IEEE Trans. Microw. Theory Tech.* **42** 1750–8
[27] Kamon M 1994 Efficient techniques for inductance extraction of complex 3-D geometries *Master's Thesis* MIT
[28] Kamon M, Silveira L, Smithhisler C and White J 1996 FastHenry USERS GUIDE Version 3.0 *A PDF Version of the Original 3-Part Postscript Version is Available from [29]* (Cambridge: MIT)
[29] Whiteley Research Inc. (available at: www.wrcad.com)
[30] Fourie C J, Wetzstein O, Ortlepp T and Kunert J 2011 Three-dimensional multi-terminal superconductive integrated circuit inductance extraction *Supercond. Sci. Technol.* **24** 125015
[31] Ruehli A E 1972 Inductance calculations in a complex integrated circuit environment *IBM J. Res. Dev.* **16** 470–81
[32] Guan B R, Wengler M J, Rott P and Feldman M J 1997 Inductance estimation for complicated superconducting thin film structures with a finite segment method *IEEE Trans. Appl. Supercond.* **7** 2776–9
[33] Fourie C J and Perold W J 2003 On using finite segment methods and images to establish the effect of gate structures on inter-junction inductances in RSFQ circuits *IEEE Trans. Appl. Supercond.* **13** 539–42
[34] Fourie C J and Perold W J 2005 Simulated inductance variations in RSFQ circuit structures *IEEE Trans. Appl. Supercond.* **15** 300–3
[35] Fourie C J, Volkmann M H and Weighill T Parallel processing to speed up FastHenry for dense multilayer layouts poster presentation at ASC14 unpublished (available at: http://staff.ee.sun.ac.za/cjfourie/pdfs/Poster_ASC14_CJF_ParallelFastHenry.pdf)
[36] Jackman K and Fourie C J 2015 Fast multicore FastHenry and a tetrahedral modeling method for inductance extraction of complex 3D geometries *2015 15th Int. Supercond. Electronics Conf. (ISEC)* pp 1–3
[37] Jackman K and Fourie C J 2016 Tetrahedral modeling method for inductance extraction of complex 3-D superconducting structures *IEEE Trans. Appl. Supercond.* **26** 0602305
[38] Fourie C J 2015 Full-gate verification of superconducting integrated circuit layouts with InductEx *IEEE Trans. Appl. Supercond.* **25** 1300209
[39] Fourie C J, Takahashi A and Yoshikawa N 2015 Fast and accurate inductance and coupling calculation for a multi-layer Nb process *Supercond. Sci. Technol.* **28** 035013
[40] Fourie C J *et al* 2019 ColdFlux superconducting EDA and TCAD tools project: overview and progress *IEEE Trans. Appl. Supercond.* **29** 1300407
[41] Fourie C J 2018 Digital superconducting electronics design tools—status and roadmap *IEEE Trans. Appl. Supercond.* **28** 1300412
[42] Sun Magnetics (available at: http://sun-magnetics.com)
[43] Khapaev M M, Kidiyarova-Shevchenko A Y, Magnelind P and Kupriyanov M Y 2001 3D-MLSI: software package for inductance calculation in multilayer superconducting integrated circuits *IEEE Trans. Appl. Supercond.* **11** 1090–3
[44] Khapaev M M, Kupriyanov M Y, Goldobin E and Siegel M 2003 Current distribution simulation for superconducting multi-layered structures *Supercond. Sci. Technol.* **16** 24–27
[45] Khapaev M M 1997 Extraction of inductances of plane thin film superconducting circuits *Supercond. Sci. Technol.* **10** 389–94
[46] Khapaev M M 2001 Inductance extraction of multilayer finite-thickness superconductor circuits *IEEE Trans. Microw. Theory Tech.* **49** 217–20
[47] Khapaev M M 3D-MLSI: Extraction of inductances of multilayer superconductor circuits (available at: http://vmbak.cs.msu.ru/sotr/vmhap/3dmlsi/3dmlsi.htm)
[48] Pegrum C, Mitchell E, Muller K, Purches W, Keenan S, Lewis C, Grancea A, Fairman P, Lazar J and Foley C 2019 Inductance extraction and simulation of small SQUID arrays and SQIFs *Eur. Conf. Appl. Supercond. EUCAS19 (Glasgow)* (unpublished)
[49] Pegrum C, Mitchell E E, Müller K H, Purches W, Keenan S, Lewis C J, Fairman P and Lazar J 2020 Simulation at 77K of SQUID and SQIF arrays: the roles of array length and average loop inductance *Appl. Supercond. Conf. ASC2020, Online Virtual Conf., Poster Presentation*
[50] Pegrum C M 2016 Cumulative internal report to CSIRO (unpublished)
[51] Khapaev M M and Kupriyanov M Y 2015 Inductance extraction of superconductor structures with internal current sources *Supercond. Sci. Technol.* **28** 055013
[52] Syms R R A, Ahmad M M, Young I R, Li Y, Hand J and Gilderdale D 2005 MEMS Helmholtz coils for magnetic resonance imaging *J. Micromech. Microeng.* **15** S1
[53] Ketchen M, Gallagher W, Kleinsasser A, Murphy S and Clem J 1985 DC SQUID flux focuser *Squid'85, Superconducting Quantum Interference Devices and Their Applications*, ed H Hahlbohm and H Lubbig (Berlin: de Gruyter) pp 865–71
[54] Drung D 2016 Introduction to Nb-based SQUID Sensors *IEEE/CSC and Esas Superconductivity News Forum* global edn, ed E L Wolf, G B Arnold, M A Gurvitch and J F Zasadzinski (available at: https://snf.ieeecsc.org/issue-no-36-april-2016)
[55] Lee J Y and Lemberger T R 1993 Penetration depth $\lambda(T)$ of $YBa_2Cu_3O_{7-\delta}$ films determined from the kinetic inductance *Appl. Phys. Lett.* **62** 2419–21
[56] Li H, Cho E Y, Cai H, Wang Y, McCoy S J and Cybart S A 2019 Inductance investigation of $YBa_2Cu_3O_{7-\delta}$ nano-slit

SQUIDs fabricated with a focused helium ion beam *IEEE Trans. Appl. Supercond.* **29** 1600404
[57] Ruffieux S, Kalaboukhov A, Xie M, Chukhar kin M, Pfeiffer C, Sepehri S, Schneiderman J F and Winkler D 2020 The role of kinetic inductance on the performance of YBCO SQUID magnetometers *Supercond. Sci. Technol.* **33** 025007
[58] Keenan S, Pegrum C, Gali Labarias M and Mitchell E E 2021 Determining the temperature-dependent London penetration depth in HTS thin films and its effect on SQUID performance *Appl. Phys. Lett.* **119** 142601
[59] Lam S K H, Cantor R, Lazar J, Leslie K E, Du J, Keenan S T and Foley C P 2013 Low-noise single-layer $YBa_2Cu_3O_{7-x}$ dc superconducting quantum interference devices magnetometers based on step-edge junctions *J. Appl. Phys.* **113** 123905
[60] Il'ichev E, Dörrer L, Schmidl F, Zakosarenko V, Seidel P and Hildebrandt G 1996 Current resolution, noise and inductance measurements on high-T_c dc SQUID galvanometers *Appl. Phys. Lett.* **68** 708–10
[61] Milliken F P, Koch R H, Brown S L, Altman R A, Gallagher W J, Haupt S G and Lathrop D K 1997 The response of high-T_c SQUID magnetometers to small changes in temperature *J. Appl. Phys.* **82** 6301–5
[62] Jewett R 1982 Josephson junctions in SPICE 2G5 *Technical Report* (Berkeley: University of California) (available at: https://ptolemy.berkeley.edu/projects/embedded/pubs/downloads/spice/josephsonJunctionsInSPICE2G5.pdf)
[63] Whiteley S R 1991 Josephson-junctions in SPICE3 *IEEE Trans. Magn.* **27** 2902–5
[64] Fang E S and Van Duzer T 1989 A Josephson integrated circuit simulator (JSIM) for superconductive electronics application *Extended Abstracts of the Int. Supercond. Electronics Conf. (ISEC'89) (Tokyo, Japan)* pp 407–10
[65] Fang E S 1991 A Josephson flash-type analog-to-digital converter and related topics in superconductive circuits *PhD Thesis* University of California, Berkeley
[66] Satchell J 1997 Stochastic simulation of SFQ logic *IEEE Trans. Appl. Supercond.* **2** 3315–18
[67] Delport J A, Jackman K, le Roux P and Fourie C J 2019 JoSIM - superconductor SPICE simulator *IEEE Trans. Appl. Supercond.* **29** 1300905
[68] Delport J A 2019 JoSIM: Superconducting circuit simulator (available at: https://github.com/JoeyDelp/JoSIM)
[69] Razmkhah S and Febvre P 2020 Joinus: a user-friendly open-source software to simulate digital superconductor circuits *IEEE Trans. Appl. Supercond.* **30** 1300807
[70] Schevchenco P 2016 PSCAN2 Superconducting circuit simulator (available at: www.pscan2sim.org)
[71] Polonsky S V, Semenov V K and Shevchenko P N 1991 PSCAN: personal superconductor circuit analyser *Supercond. Sci. Technol.* **4** 667–70
[72] Polonsky S, Shevchenko P, Kirichenko A, Zinoviev D and Rylyakov A 1997 PSCAN96: new software for simulation and optimization of complex RSFQ circuits *IEEE Trans. Appl. Supercond.* **7** 2685–9
[73] Kornev V K and Arzumanov A V 1997 Numerical simulation of Josephson-junction system dynamics in the presence of thermal noise *Inst. Phys. Conf. Ser.* pp 627–30
[74] Kornev V K and Arzumanov A V 1998 Josephson-junction oscillation spectral linewidth for some phase-locked multijunction systems *J. Phys. IV France* **8** 279–82
[75] Akgun A and Razmkhah S 2022 PySQIF, a statistical analysis tool for bi-SQUID magnetometers *J. Phys.: Conf. Ser.* **2323** 012026
[76] Kornev V K, Soloviev I I, Klenov N V and Mukhanov O A 2009 Bi-SQUID: a novel linearization method for dc SQUID voltage response *Supercond. Sci. Technol.* **22** 114011
[77] Accellera systems initiative (available at: www.accellera.org)
[78] `josephson_contact.va` (available at: www.eda-twiki.org/twiki/pub/VerilogAMS/AmsExamplesSDM/josephson_contact.va)
[79] Advanced Design System (ADS), Keysight Technologies (available at: www.keysight.com/en/pc-1297113/advanced-design-system-ads)
[80] Zhang T, Pegrum C, Du J and Guo Y J 2017 Simulation and measurement of a Ka-band HTS MMIC Josephson junction mixer *Supercond. Sci. Technol.* **30** 015008
[81] Zhang T, Gao X, Wang W, Du J, Pegrum C and Guo Y J 2017 A 36 GHz HTS MMIC Josephson mixer—simulation and measurement *IEEE Trans. Appl. Supercond.* **27** 1502405
[82] Quite universal circuit simulator *Qucs* (available at: http://qucs.sourceforge.net)
[83] SIMetrix (available at: www.simetrix.co.uk)
[84] DesignSoft TINA (available at: www.tina.com)
[85] van Zyl D S 2010 SQUID detected low-field NMR for the evaluation of internal fruit quality *Master's Thesis* University of Stellenbosch
[86] Whiteley S 2018 WRspice reference manual, section 2.15.3.2 (available at: www.wrcad.com/manual/wrsmanual/node102.html)
[87] Jeffery M, Xie P Y, Whiteley S R and Duzer T V 1999 Monte Carlo and thermal noise analysis of ultra-high-speed high temperature superconductor digital circuits *IEEE Trans. Appl. Supercond.* **9** 4095–8
[88] Matlab (available at: www.mathworks.com/products/matlab.html)
[89] GNU Octave is in repositories for most Linux distributions and can be used in place of Matlab for most of the procedures described in this Review (available at: www.gnu.org/software/octave/about.html)
[90] O'Haver T 2018 A pragmatic introduction to signal processing (available at: https://terpconnect.umd.edu/~toh/spectrum/TOC.html)
[91] Schmid H 2012 How to use the FFT and Matlab's pwelch function for signal and noise simulations and measurements (available at: www.schmid-werren.ch/hanspeter/publications/2012fftnoise.pdf)
[92] Hannam K E, Mitchell E E, Yuan M, Keenan S T, Zhao B and Foley C P 2016 High-Tc step-edge Josephson junction arrays: comparison of simulated and experimental voltage responses *IEEE Trans. Appl. Supercond.* **26** 1601905
[93] Mitchell E E, Hannam K E, Lazar J, Leslie K E, Lewis C J, Grancea A, Keenan S T, Lam S K H and Foley C P 2016 2D SQIF arrays using 20 000 YBCO high R_n Josephson junctions *Supercond. Sci. Technol.* **29** 06LT01
[94] Oppenländer J, Häussler C, Träuble T, Caputo P, Tomes J, Freisch A and Schopohl N 2003 Two dimensional superconducting quantum interference filters *IEEE Trans. Appl. Supercond.* **13** 771–4
[95] Zhang T, Du J, Guo Y J and Sun X 2012 Design and integration of HTS filters with a Josephson device *Supercond. Sci. Technol.* **25** 105014
[96] Zhang T, Du J, Guo Y and Sun X 2013 A 7 – 8.5 GHz high performance MMIC HTS Josephson mixer *IEEE Microw. Wirel. Compon. Lett.* **23** 427–9
[97] Du J, Zhang T, Guo Y J and Sun X W 2013 A high-temperature superconducting monolithic microwave integrated Josephson down-converter with high conversion efficiency *Appl. Phys. Lett.* **102** 212602
[98] Du J, Bai D D, Zhang T, Guo Y J, He Y S and Pegrum C M 2014 Optimised conversion efficiency of a HTS MMIC Josephson down-converter *Supercond. Sci. Technol.* **27** 105002
[99] Du J, Wang J, Zhang T, Bai D, Guo Y and He Y 2015 Demonstration of a portable HTS MMIC microwave

receiver front-end *IEEE Trans. Appl. Supercond.* **25** 1500404
[100] Zhang T, Du J, Wang J, Bai D, Guo Y and He Y 2015 30 GHz HTS receiver front-end based on monolithic Josephson mixer *IEEE Trans. Appl. Supercond.* **25** 1400605
[101] Du J, Pegrum C M, Gao X, Weily A R, Zhang T, Guo Y J and Foley C P 2017 Harmonic mixing using a HTS step-edge Josephson junction at 0.6 THz frequency *IEEE Trans. Appl. Supercond.* **27** 1500905
[102] Du J, Weily A R, Gao X, Zhang T, Foley C P and Guo Y J 2016 HTS step-edge Josephson junction terahertz harmonic mixer *Supercond. Sci. Technol.* **30** 024002
[103] Gao X, Du J, Zhang T and Guo Y J 2017 Design of a monolithic-integrated circularly-polarized antenna-coupled high-T_c superconducting terahertz harmonic mixer *IEEE-APS Topical Conf. Antennas Propagation Wireless Communications (APWC17)* pp 324–5
[104] Gao X, Du J, Zhang T and Guo Y J 2017 Noise and conversion performance of a high-T_c superconducting Josephson junction mixer at 0.6 THz *Appl. Phys. Lett.* **111** 192603
[105] Gao X, Zhang T, Du J, Weily A R, Guo Y J and Foley C P 2017 A wideband terahertz high-T_c superconducting Josephson-junction mixer: electromagnetic design, analysis and characterization *Supercond. Sci. Technol.* **30** 095011
[106] Gao X, Zhang T, Du J and Guo Y J 2018 Design, modelling and simulation of a monolithic high-T_c superconducting terahertz mixer *Supercond. Sci. Technol.* **31** 115010
[107] Gao X, Du J, Zhang T and Guo Y J 2018 High-T_c superconducting fourth-harmonic mixer using a dual-band terahertz on-chip antenna of high coupling efficiency *IEEE Trans. Terahertz Sci. Technol.* **9** 55–62
[108] Pegrum C, Zhang T, Du J and Guo Y J 2016 Simulation of HTS Josephson mixers *IEEE Trans. Appl. Supercond.* **26** 1500905
[109] Hansma P K 1973 Superconducting single-junction interferometers with small critical currents *J. Appl. Phys.* **44** 4191–4
[110] Giffard R, Webb R and Wheatley J 1972 Principles and methods of low-frequency electric and magnetic measurements using an rf-biased point-contact superconducting device *J. Low Temp. Phys.* **6** 533–610
[111] Ryhänen T, Seppä H, Ilmoniemi R and Knuutila J 1989 SQUID magnetometers for low-frequency applications *J. Low Temp. Phys.* **76** 287–386
[112] Ehnholm G 1977 Theory of the signal transfer and noise properties of the rf SQUID *J. Low Temp. Phys.* **29** 1–27
[113] Chesca B 1998 Theory of RF SQUIDs operating in the presence of large thermal fluctuations *J. Low Temp. Phys.* **110** 963–1001
[114] Kleiner R, Koelle D and Clarke J 2007 A numerical treatment of the rf SQUID: I. general properties and noise energy *J. Low Temp. Phys.* **149** 230–60
[115] Blackburn J A 2007 Circuit for precision simulation of a capacitive Josephson junction *J. Appl. Phys.* **101** 093908
[116] Henry R W and Prober D E 1981 Electronic analogs of double-junction and single-junction SQUIDs *Rev. Sci. Instrum.* **52** 902–14
[117] Blackburn J A, Wu B and Smith H J T 1988 Analog simulation of superconducting loops containing one or 2 Josephson-junctions *J. Appl. Phys.* **64** 3112–18
[118] Heath T and Wiesenfeld K 1998 Mutual entrainment of two nonlinear oscillators *Am. J. Phys.* **66** 860–6
[119] Chang W H 1981 Numerical calculation of the inductances of a multi-superconductor transmission line system *IEEE Trans. Magn.* **17** 764–6
[120] Bunyk P and Rylov S 1993 Automated calculation of mutual inductance matrices of multilayer superconductor integrated circuits *Ext. Abstr. 4th Int. Supercond. Electron. Conf.* (Boulder, CO: *ISEC93)* p 62
[121] (Available at: https://github.com/coldlogix/lmeter)
[122] Mitchell E E, Tilbrook D L, MacFarlane J C and Foley C P 2003 Experimental determination of HTS dc-SQUID amplifier inductance and noise performance *IEEE Trans. Appl. Supercond.* **13** 849–52
[123] Doyle S 2008 Lumped element kinetic inductance detectors *PhD Thesis* Cardiff University
[124] Babaei Brojeny A A, Mawatari Y, Benkraouda M and Clem J R 2002 Magnetic fields and currents for two current-carrying parallel coplanar superconducting strips in a perpendicular magnetic field *Supercond. Sci. Technol.* **15** 1454–66
[125] Brandt E H 1997 Susceptibility of superconductor disks and rings with and without flux creep *Phys. Rev.* B **55** 14513–26
[126] Babaei Brojeny A A and Clem J R 2003 Magnetic-field and current-density distributions in thin-film superconducting rings and disks *Phys. Rev.* B **68** 174514
[127] Anon Circular of the National Bureau of Standards C74 Radio Instruments and Measurements 1924 Reprinted 1937 with corrections and omissions
[128] Rosa E B and Grover F W 1916 *Formulas and Tables for the Calculation of Mutual- and Self-Inductance Bulletin of the Bureau of Standards* vol 8 3rd ed (Washington: Bureau of Standards) also known as Scientific Paper 169 (S169) pp 1–237
[129] Grover F W 2004 *Inductance Calculations* (Mineola, NY: Dover Phoenix)
[130] Du Z S, Whiteley S R and Van Duzer T 1998 Inductance calculation of 3D superconducting structures *Appl. Supercond.* **6** 519–23
[131] Oppenländer J, Caputo P, Häussler C, Träuble T, Tomes J, Friesch A and Schopohl N 2003 Effects of magnetic field on two-dimensional superconducting quantum interference filters *Appl. Phys. Lett.* **83** 969–71